scientific reports

Check for updates

OPEN

Prediction of bearing capacity of ring footings on cohesive frictional soils using Terzaghi stability factors and Kolmogorov Arnold networks

Tran Vu-Hoang[1], Tan Nguyen[2]✉, Jim Shiau[3], Duy Ly-Khuong[4,5] & Hung-Thinh Pham-Tran[1]

This study investigates the bearing capacity of ring footings on frictional–cohesive soils under surcharge by analyzing three stability factors i.e., F_c, F_q, and F_γ, based on Terzaghi's principle of superposition. These factors are governed by two key inputs: the soil's internal friction angle (□) and the geometric ratio of the inner radius to the footing width (r_1/B). Advanced predictive models are developed by integrating finite element limit analysis (FELA) with an adaptive meshing technique and a data-driven Kolmogorov–Arnold Network (KAN). Building upon recent applications of KAN in geotechnical modeling, this study advances its use by demonstrating superior predictive accuracy and interpretability compared with traditional Artificial Neural Networks. A closed-form representation of the stability factors is derived from the trained KAN model, offering an efficient and transparent means for estimating bearing capacity. The optimized KAN framework achieved high coefficients of determination and low root mean square errors for both training and testing phases. Sensitivity and feature-importance analyses confirmed that □ exerts the dominant influence on stability, whereas r_1/B has a secondary effect. The results enhance the mechanistic understanding of ring-footing behavior on frictional–cohesive soils under surcharge and provide practical guidance for foundation design across diverse soil conditions.

Keywords Ultimate bearing capacity, Terzaghi's principle of superposition, Finite element limit analysis (FELA), Kolmogorov-Arnold networks (KAN), Closed-form solution, Sensitivity analysis

Ring footings are essential in the foundation design for various structures, including silos, storage tanks, chimneys, cooling towers, bridge piers, and transmission towers. Their symmetrical geometry makes them a preferred choice in engineering, as it leads to material efficiency and cost savings compared to traditional circular footings[1]. This efficiency arises because ring footings require less material to achieve similar load-bearing capacities. However, designing and analyzing ring footings requires a thorough understanding of their bearing capacity and load-settlement behavior in different soil conditions. Over the years, extensive research has been conducted in this field, employing both analytical and numerical methods to explore the behavior of ring footings[2].

The investigation of load-settlement response and contact pressure distribution under flexible and rigid ring footings began with seminal studies by Fisher[3], Egorov[4], Egorov and Nichiporovich[5]. Fischer[3] provided analytical solutions for the settlement of a flexible ring plate on an elastic isotropic half-space, while Egorov employed integral equations to determine the settlement and reactive pressure distribution beneath rigid ring footings. These foundational studies paved the way for understanding the basic behavior of ring footings under load. Further research by Milovic[6] offered additional insights into stress and displacement calculations beneath flexible ring foundations using linear elastic analysis and the finite element method (FEM). Milovic's research concentrated on evaluating how soil properties and footing geometry influence the performance of ring footings. During this period, significant contributions were made by field tests conducted by researchers such as Al-Sanad et al.[7] and Ismael[8]. Al-Sanad et al.[7] investigated the load-deformation responses of ring footings in dense

[1]Faculty of Civil Engineering, Ton Duc Thang University, Ho Chi Minh City, Vietnam. [2]Smart Computing in Civil Engineering Research Group, Faculty of Civil Engineering, Ton Duc Thang University, Ho Chi Minh City, Vietnam. [3]School of Engineering, University of Southern Queensland, Toowoomba, QLD 4350, Australia. [4]Laboratory for Computational Mechanics, Institute for Computational Science and Artificial Intelligence, Van Lang University, Ho Chi Minh City, Viet Nam. [5]Faculty of Civil Engineering, Van Lang School of Technology, Van Lang University, Ho Chi Minh City, Viet Nam. ✉email: nguyentan@tdtu.edu.vn

cemented sands, while Ismael studied these responses in natural clayey deposits. These field studies validated the theoretical and numerical models developed in earlier research.

The ultimate bearing capacity of ring footings has been a key focus of numerous studies, employing various methodologies to derive bearing capacity factors. Saha[9] conducted model tests to investigate the load-bearing capacity of ring footings. Boushehrian and Hataf[10], Zhao and Wang[11] used finite element and finite difference methods, respectively, to calculate bearing capacity factors for different soil conditions. Keshavarz and Kumar[13] employed the SCM to compute the bearing capacity of smooth and rough ring foundations. Their analysis incorporated stress singularities at the inner and outer edges of the ring footing and presented bearing capacity factors (N_c, N_q, and N_γ) as a function of the soil's internal friction angle (ϕ) and the ratio (r_i/r_o) of inner to outer radii of the footing. Seyedi Hosseininia[2] expanded on these studies by determining all three bearing capacity factors (N_c, N_q, and N_γ) for ring footings using the finite difference method. His work included the effects of footing roughness and provided practical formulas for estimating bearing capacity, aligning with the superposition principles of Terzaghi's classical equation. Hosseininia's research addressed a gap in the literature regarding the comprehensive evaluation of all bearing capacity factors for ring footings, offering a more holistic understanding of their performance.

Substantial progress has been made in analyzing ring footings using finite element methods. Kumar and Chakraborty[12] computed bearing capacity factors for smooth and rough ring footings using lower bound finite elements and linear optimization techniques. Their research highlighted the influence of footing roughness and the ring radii ratio on the collapse load, offering valuable design insights for engineers. Tang and Phoon[14] advanced this field by employing finite-element formulation of the lower bound theorem to determine the bearing capacity of ring foundations on dense sand. Their study incorporated the Bolton strength–dilatancy relation to account for stress level effects on the soil's friction angle. The results were validated using centrifuge model tests, which showed good agreement with theoretical predictions for solid circular footings. However, significant discrepancies were observed for ring foundations with a radii ratio exceeding 0.5, leading Tang and Phoon to propose an alternative method to address these differences.

Recent advances in machine learning (ML) and artificial neural networks (ANNs) have significantly enhanced predictive modeling in geotechnical engineering[15–18]. Nguyen et al.[19] combined finite element limit analysis (FELA) with ANNs to predict the bearing capacity of ring footings in anisotropic clays, considering the anisotropic and depth-increasing undrained shear strength of clays. Their hybrid model highlighted the radius ratio as the most influential factor, followed by embedment ratio, the rate of increase of undrained shear with depth, and the anisotropy ratio. Vali et al.[20] further developed this field by using a deep neural network (DNN) on an extensive dataset of 80,000 samples to predict bearing capacity, considering factors such as clay undrained shear strength, soil friction angle, radius ratio, sand layer thickness, and footing-soil interface.

Despite these advancements, no study has yet utilized Kolmogorov-Arnold Networks (KAN) in the context of ring footing analysis. Kolmogorov-Arnold Networks (KANs) are inspired by the Kolmogorov-Arnold representation theorem[21,22]. Unlike Multilayer Perceptrons (MLPs) which use fixed activation functions at the nodes, KANs use learnable activation functions on the edges. Each weight in KANs is a learnable one-dimensional function, typically a spline, eliminating the need for linear weight matrices. Nodes in KANs sum incoming signals without non-linearities, resulting in smaller computation graphs compared to MLPs. This structure allows KANs to outperform MLPs in accuracy and interpretability, achieving comparable results with smaller sizes and exhibiting faster neural scaling laws[23].

While many traditional ML techniques—such as support vector regression, polynomial regression, and decision-tree ensembles—have been widely applied in bearing-capacity modeling, they rely on fixed activation mechanisms and rigid parametric assumptions that limit their ability to capture strongly coupled, nonlinear soil–structure interactions. These models also lack the transparency required to interpret how input parameters (e.g., ϕ and r_1/B) influence bearing-capacity factors. In contrast, KAN employs learnable spline-based functional connections that can dynamically adapt to complex nonlinear relationships while maintaining interpretability and parameter efficiency. This capability makes KAN particularly suitable for problems in geotechnical engineering where nonlinear dependencies dominate and physical interpretability remains essential.

Known for their ability to approximate complex functions, KANs offer a novel approach to modeling the bearing capacity factors (F_c, F_q, and F_γ) of ring footings on frictional-cohesive soils under surcharge. This study seeks to address this gap by applying KAN for the first time in geotechnical engineering. By doing so, it establishes a compact, transparent, and physically consistent alternative to conventional data-driven approaches, bridging the divide between numerical simulation and engineering design. The innovative application of Kolmogorov-Arnold Networks[23] in this research marks an important step forward, providing a comprehensive and advanced method for understanding the behavior of ring footings. By integrating traditional finite element methods with cutting-edge machine learning techniques, this research offers reliable design guidelines and contributes to the advancement of geotechnical engineering practices.

Problem formulation and FELA model

Figure 1 illustrates the problem definition of a ring footing under axisymmetric condition. The ring footing has a width of B defined as the difference between the outer radius (r_2) and the inner radius (r_1). When $r_1 = 0$ and $r_2 = B$, it forms a solid circular footing. The ultimate bearing capacity (P_u) of a ring footing is calculated similarly to Terzaghi's bearing capacity equation as follows:

$$P_u = \frac{Q_u}{\pi(2r_1B + B^2)} = cF_c + qF_q + \gamma BF\gamma \tag{1}$$

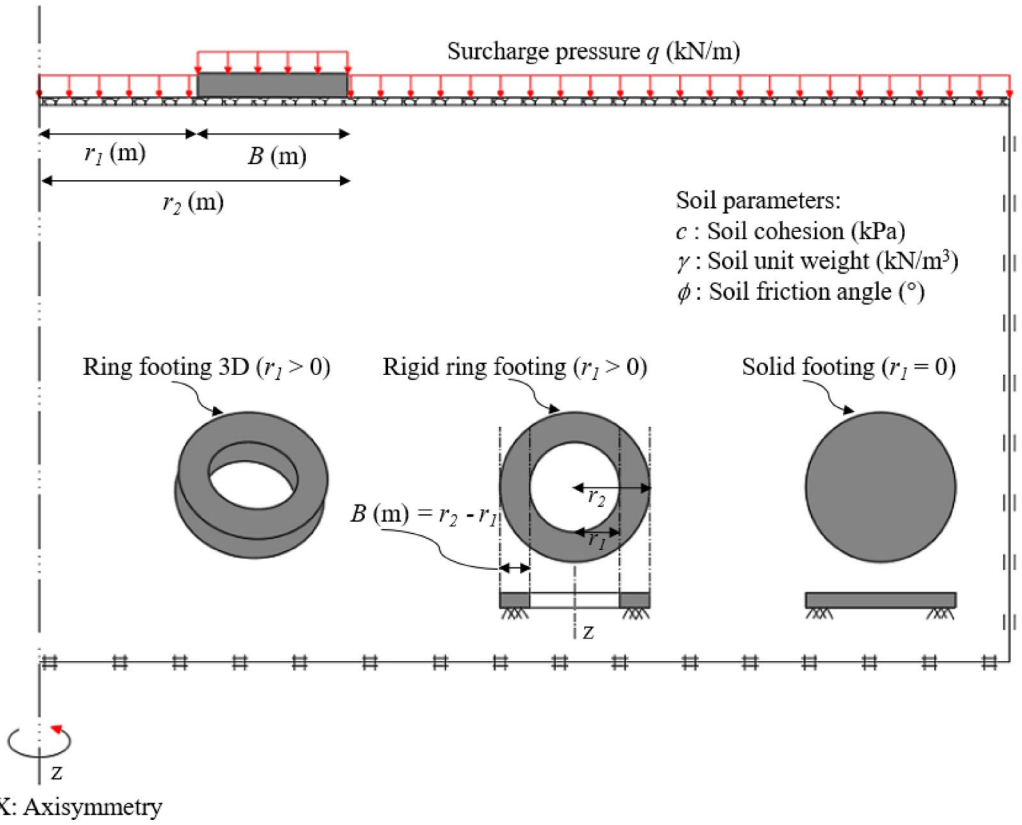

Fig. 1. Problem definition of a ring footing under axisymmetric condition.

where, Q_u is the ultimate collapse load, c denotes effective cohesion, q signifies potential surcharge loading on the ground surface, and γ represents soil unit weight. Terzaghi's principle of linear superposition, a widely accepted practice in design calculations, is adopted to determine the ultimate bearing capacity (P_u) using the bearing capacity factors (F_c, F_q, and F_γ). This approach provides a conservative estimate of P_u, meaning the actual collapse load usually exceeds the value determined by this method[12,24,25].

As discussed in Shiau et al.[26], Nguyen and Shiau[27], to derive the factor F_c, the analytical process begins by setting both the unit weight ($\gamma = 0$) and surcharge pressure ($q = 0$) to zero. Subsequently, F_c is calculated using the reduced Eq. 1: $F_c = P_u/c$. Similarly, for computing the factor F_q, a comparable approach is utilized where cohesion ($c = 0$) and unit weight ($\gamma = 0$) are both set to zero in Eq. 1. Through this process, F_q is determined using $F_q = P_u/qB$. Likewise, the determination of the factor F_γ involves setting both cohesion ($c = 0$) and surcharge pressure ($q = 0$) to zero in Eq. 1 to find P_u. Once P_u is determined, F_γ is computed using $F_\gamma = P_u/\gamma B^2$.

The computation of P_u, and thereafter F_c, F_q, and F_γ, are performed sequentially in this study. An adaptive meshing technique is utilized to discretize the analyzed domain using OptumCE G2[28]. Figure 2 illustrates a typical adaptive mesh configuration along with its boundary conditions. Standard boundary conditions are applied: both sides are fixed in the normal direction, while the bottom side is fixed in both directions. The ground surface remains free, and a rigid block is positioned at the anchor location with a perfect rough interface condition.

This study employs plastic limit theorems, encompassing both upper bound (UB) and lower bound (LB) analyses. In the lower bound theorem, the objective is to achieve an equilibrium stress distribution that balances applied loads without violating yield criteria. Conversely, the upper bound theorem explores patterns of plastic deformation where external work rates exceed internal plastic dissipation, indicating potential collapse. These theoretical bounds provide a comprehensive understanding of material behavior and its load-bearing capacity for assessing soil stability issues. Further details on the application of plastic limit theorems can be found in OptumCE G2[28].

Analysis of bearing capacity stability factors (F_c, F_q, and F_γ)

Of note, Figs. 3, 4, 5, 6, 7, 8, 9, 10, 11, 12, 13, 14, 15, 16, 17, 18, 19, 20 and 21 use $r_1/B = 0$, 2, 5 to illustrate representative failure mechanisms and stress distributions under different geometric configurations. These values were chosen to qualitatively visualize distinct collapse modes. In contrast, Tables 1, 2 and 3 adopt $r_1/B = 0$, 1, 3, which are commonly reported in the literature, enabling direct quantitative comparison and validation. The difference serves visualization versus verification purposes, without affecting the consistency or conclusions of the analysis.

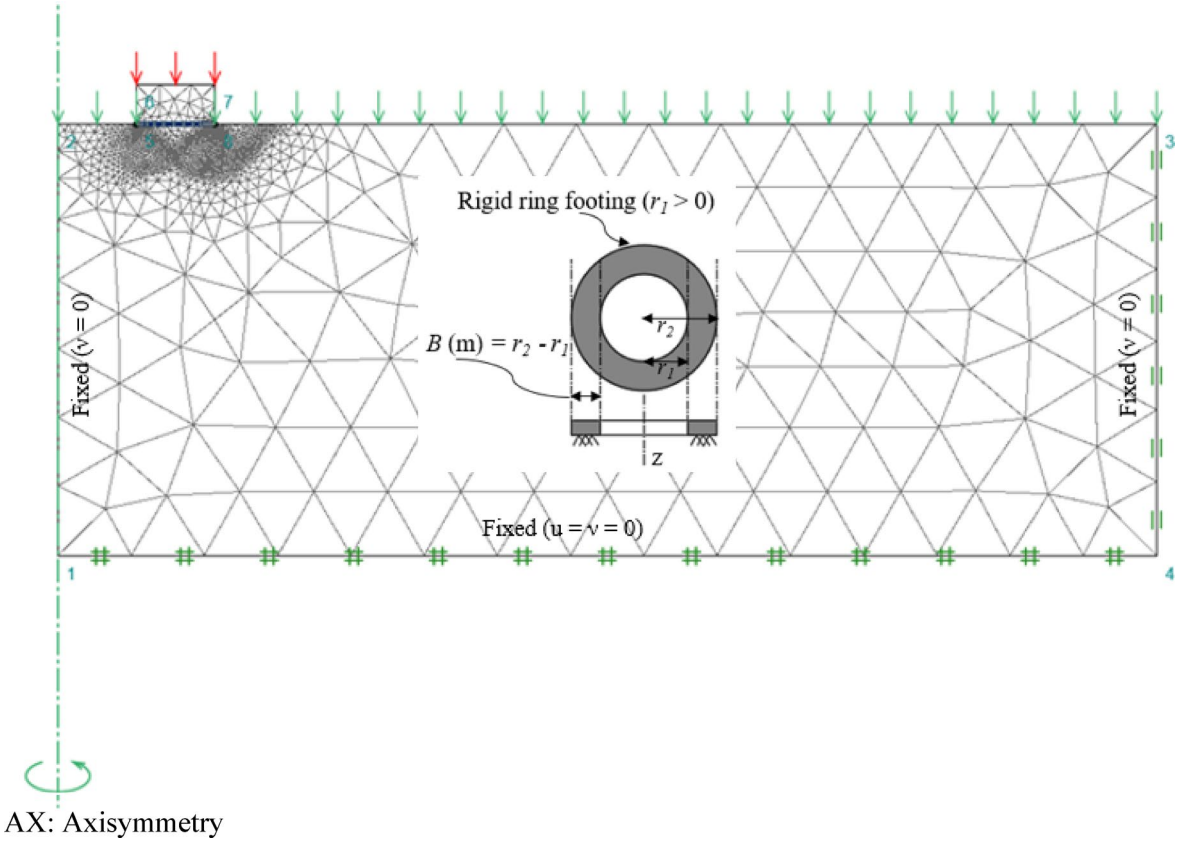

Fig. 2. A typical adaptive mesh and its boundary conditions for ring footings.

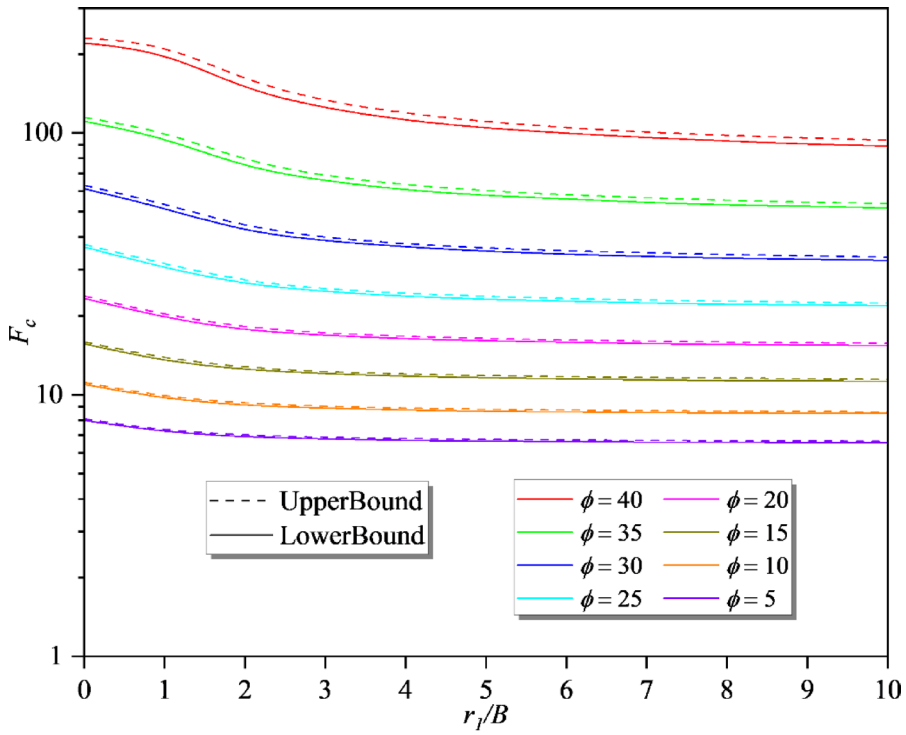

Fig. 3. The factor F_c.

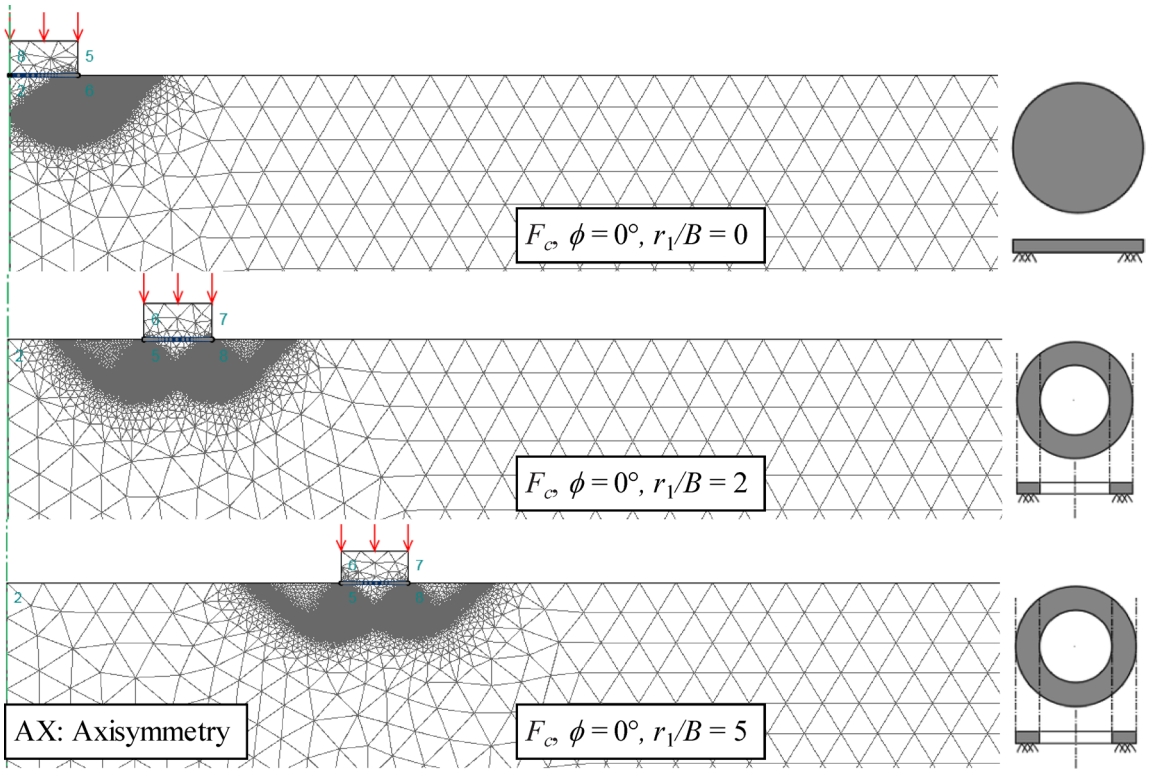

Fig. 4. Typical adaptive meshes for the analysis of F_c (r_1/B = 0, 2, and 5; $\phi = 0°$).

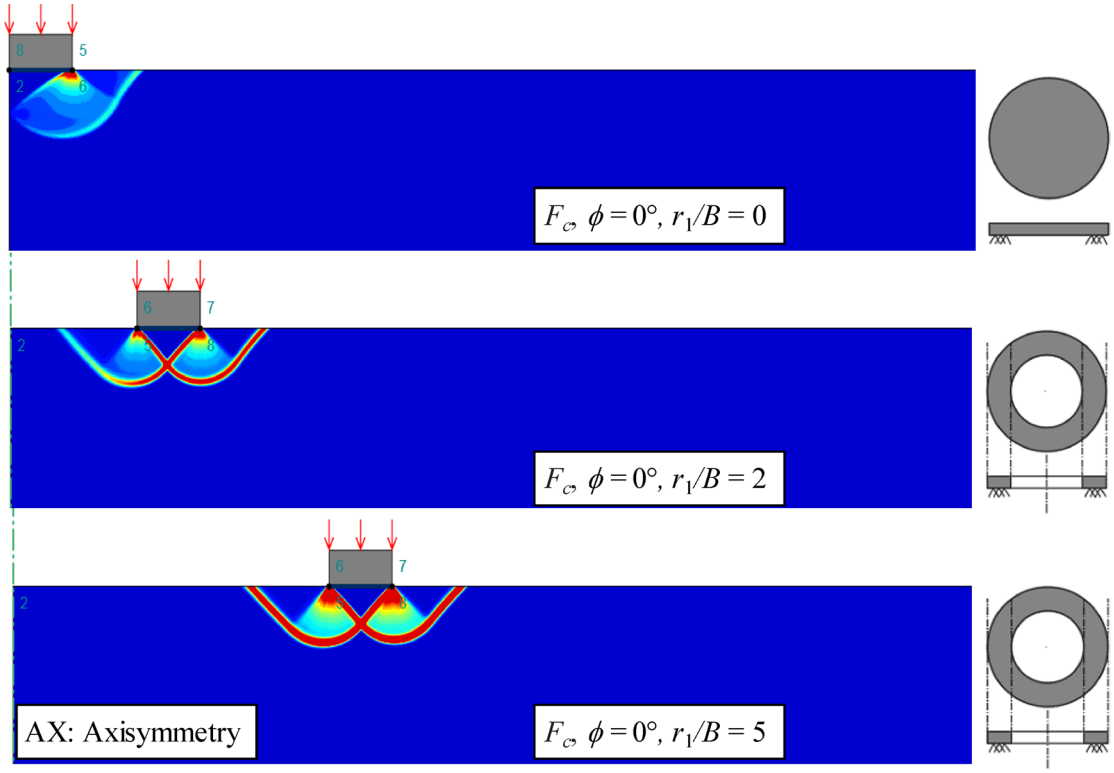

Fig. 5. Typical failure mechanisms for the analysis of F_c (r_1/B= 0, 2, and 5; $\phi = 0°$).

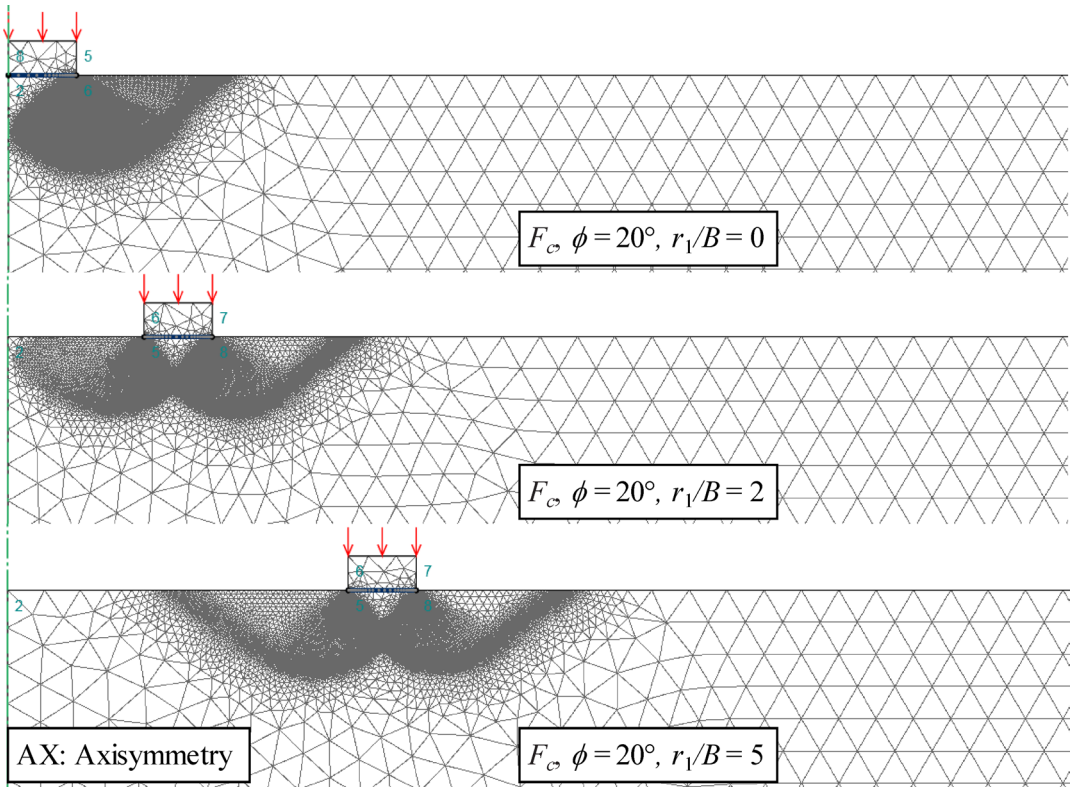

Fig. 6. Typical adaptive meshes for the analysis of F_c (r_1/B= 0, 2, and 5;ϕ =20°).

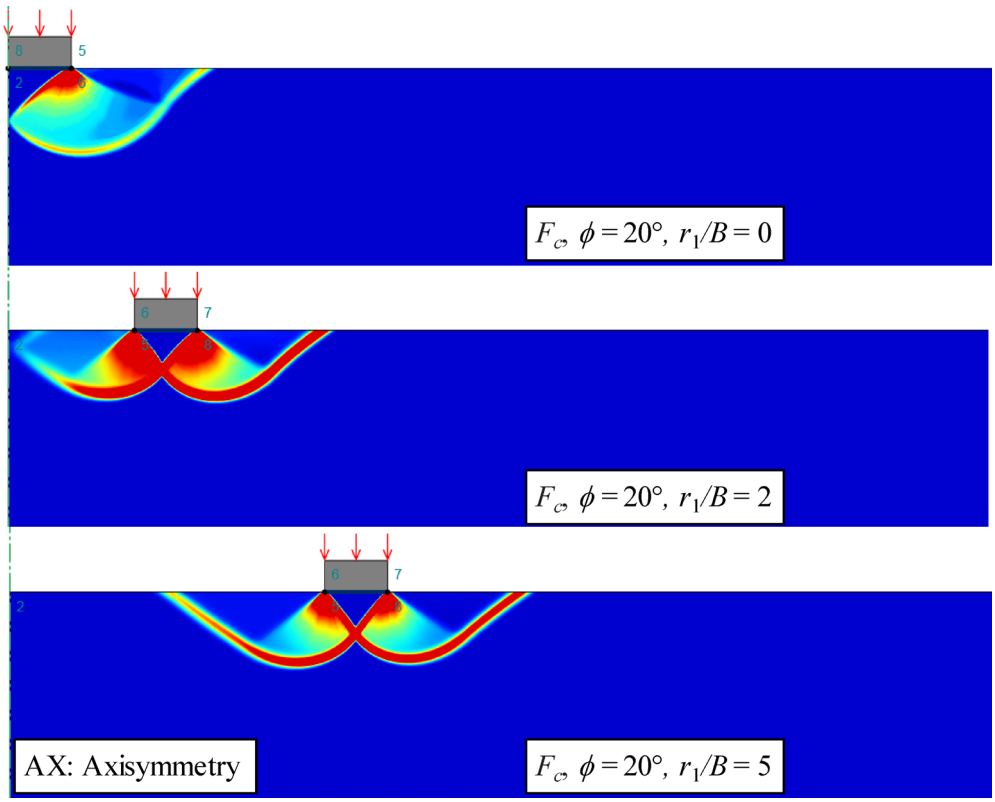

Fig. 7. Typical failure mechanisms for the analysis of F_c (r_1/B= 0, 2, and 5;ϕ =20°).

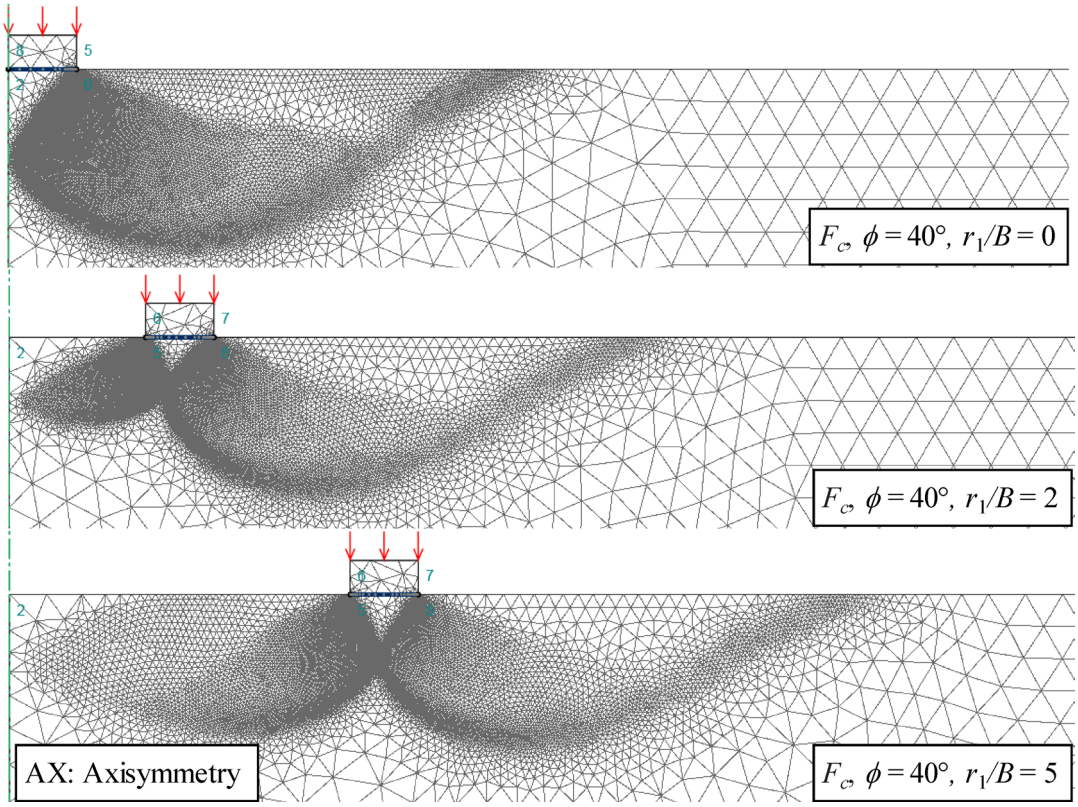

Fig. 8. Typical adaptive meshes for the analysis of F_c (r_1/B= 0, 2, and 5;ϕ = 40°).

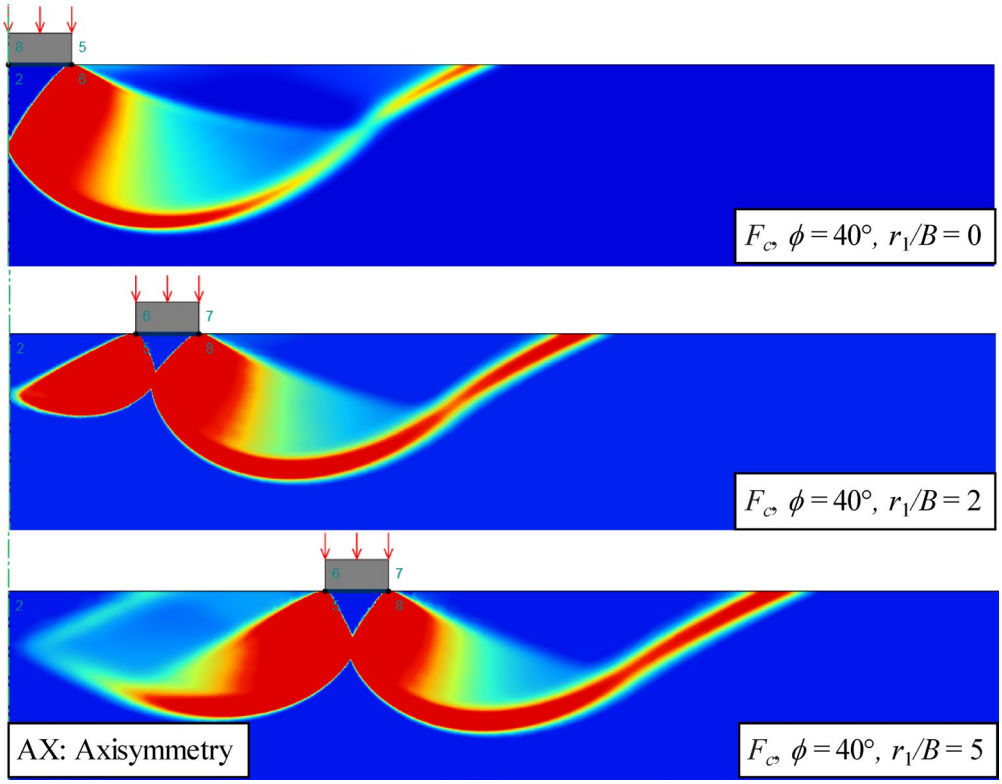

Fig. 9. Typical failure mechanisms for the analysis of F_c (r_1/B= 0, 2, and 5;ϕ = 40°).

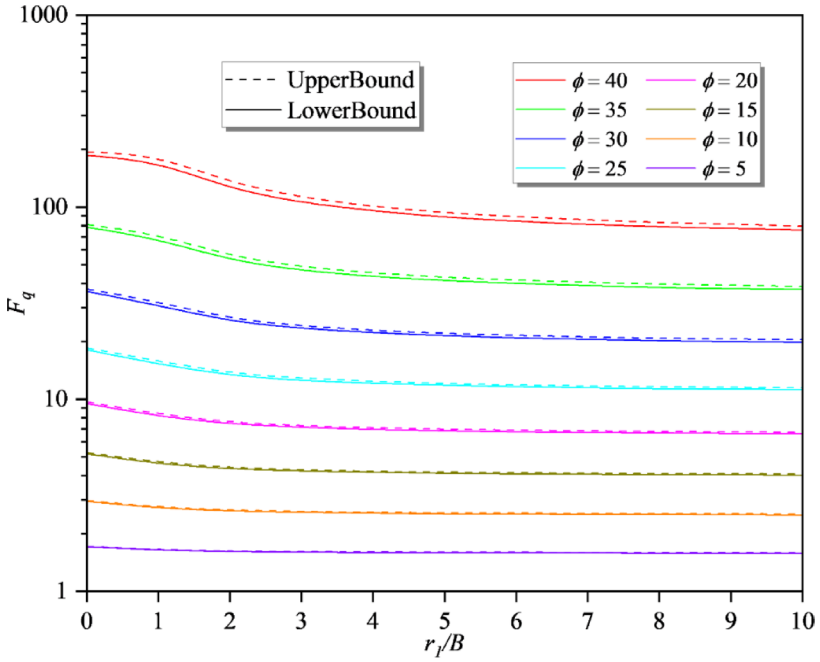

Fig. 10. The factor F_q.

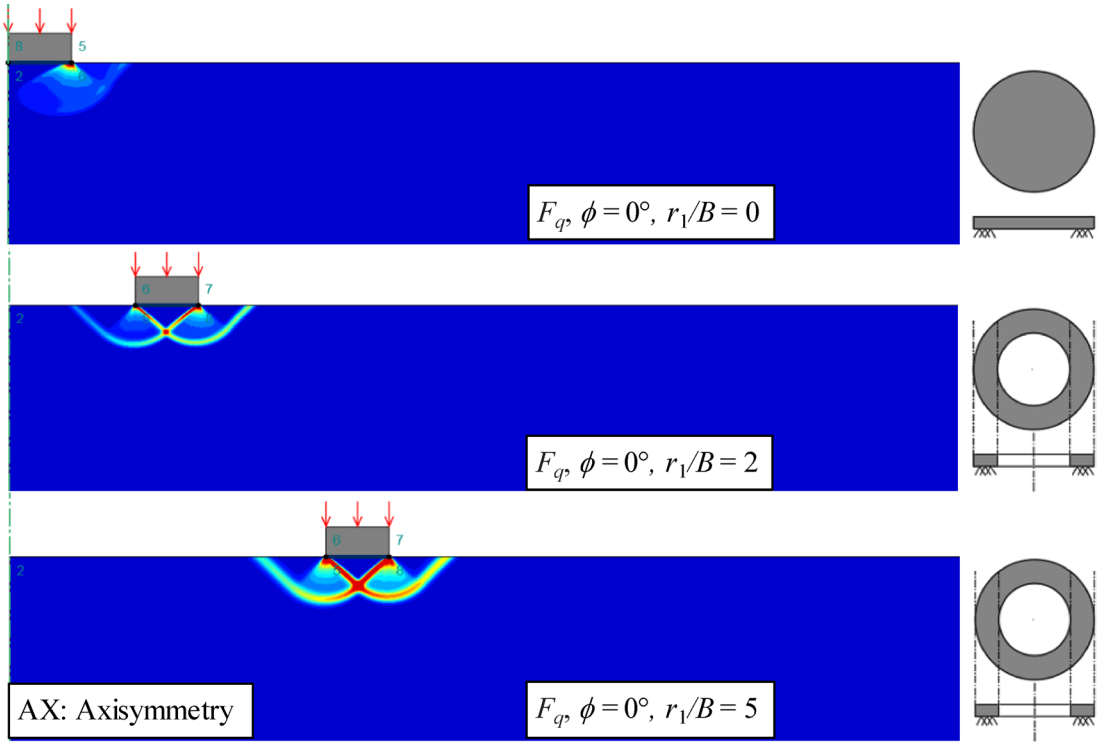

Fig. 11. Typical adaptive meshes for the analysis of F_q (r_1/B= 0, 2, and 5;$\phi = 0°$).

Cohesion factors (F_c)

Shown in Fig. 22 is the variation of F_c with r_1/B for different values of internal friction angle (ϕ). It reveals significant trends and interactions between the internal friction angle (ϕ) and the ratio of the inner radius to the width of the ring footing (r_1/B) on the cohesion factor (F_c). The internal friction angle (ϕ) ranges from 0 to 40 degrees, while r_1/B varies from 0 to 10. As ϕ increases, F_c also increases significantly, indicating a strong positive correlation. Conversely, for a fixed ϕ increasing r_1/B generally leads to a decrease in F_c, suggesting an

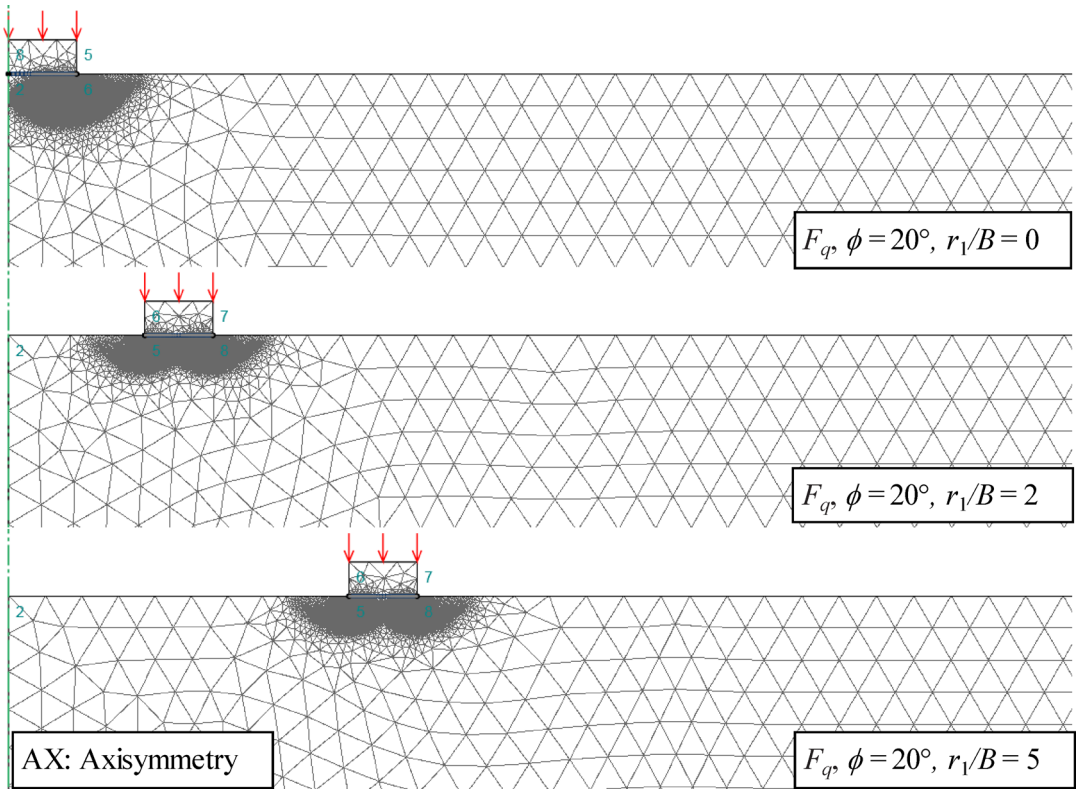

Fig. 12. Typical failure mechanisms for the analysis of F_q (r_1/B= 0, 2, and 5;ϕ= 0°).

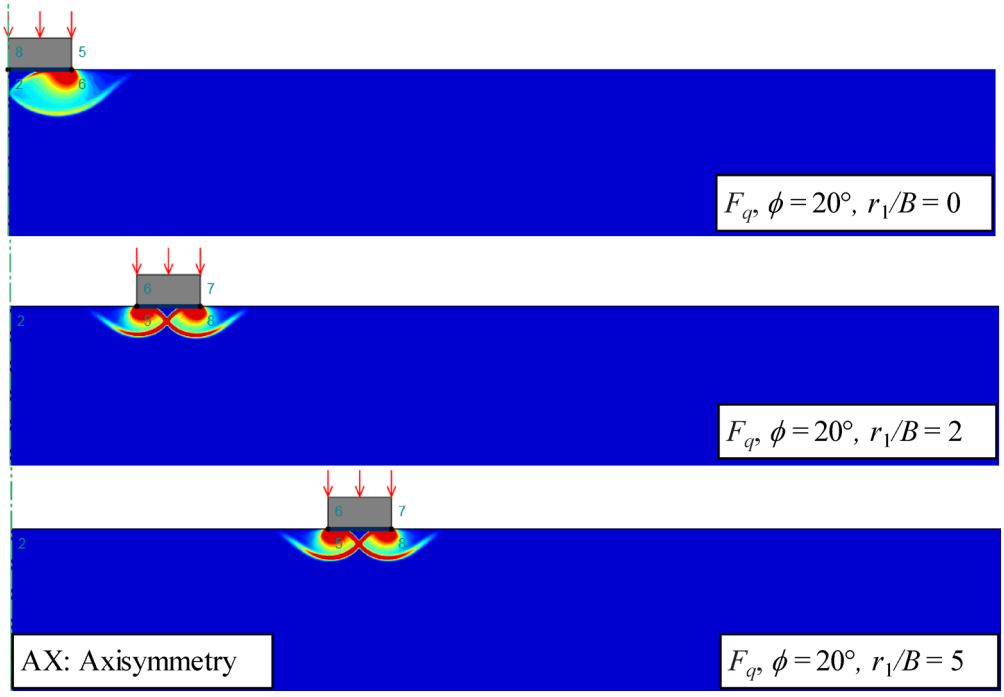

Fig. 13. Typical adaptive meshes for the analysis of F_q ($r_1/B = 0$, 2, and 5; $\phi = 20°$).

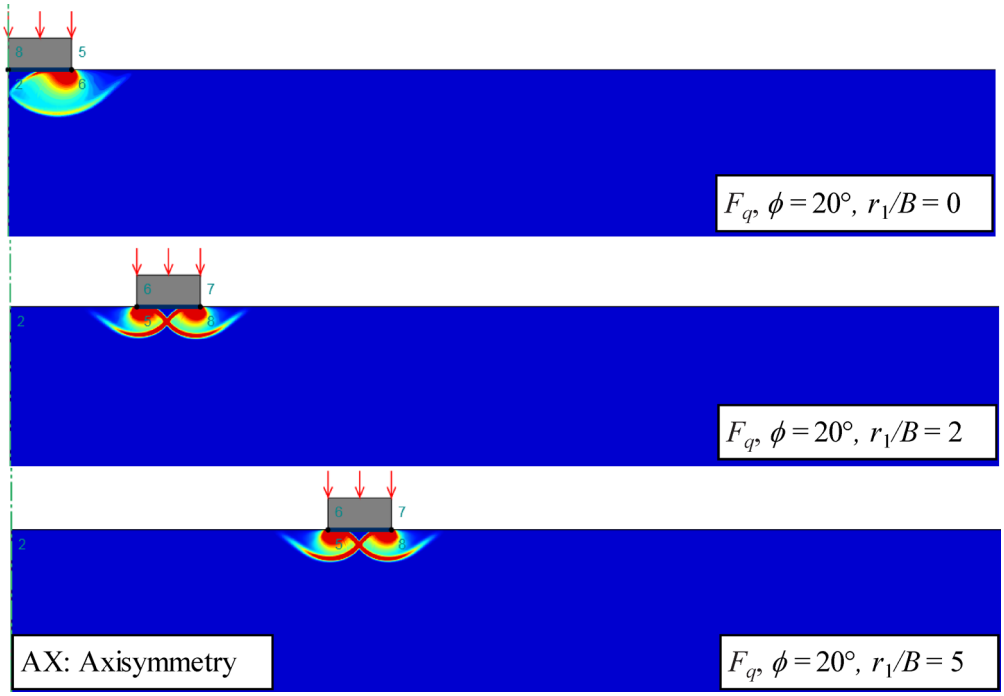

Fig. 14. Typical failure mechanisms for the analysis of F_q ($r_1/B = 0$, 2, and 5; $\phi = 20°$).

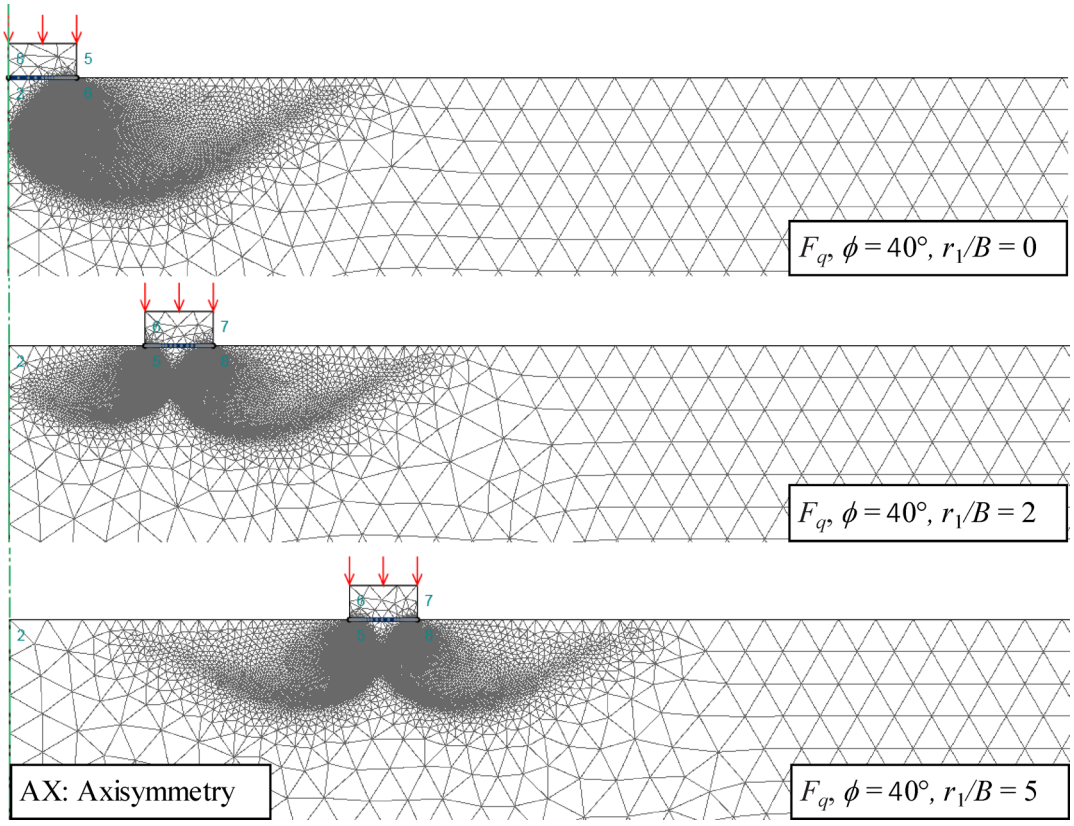

Fig. 15. Typical adaptive meshes for the analysis of F_q ($r_1/B = 0$, 2, and 5; $\phi = 40°$).

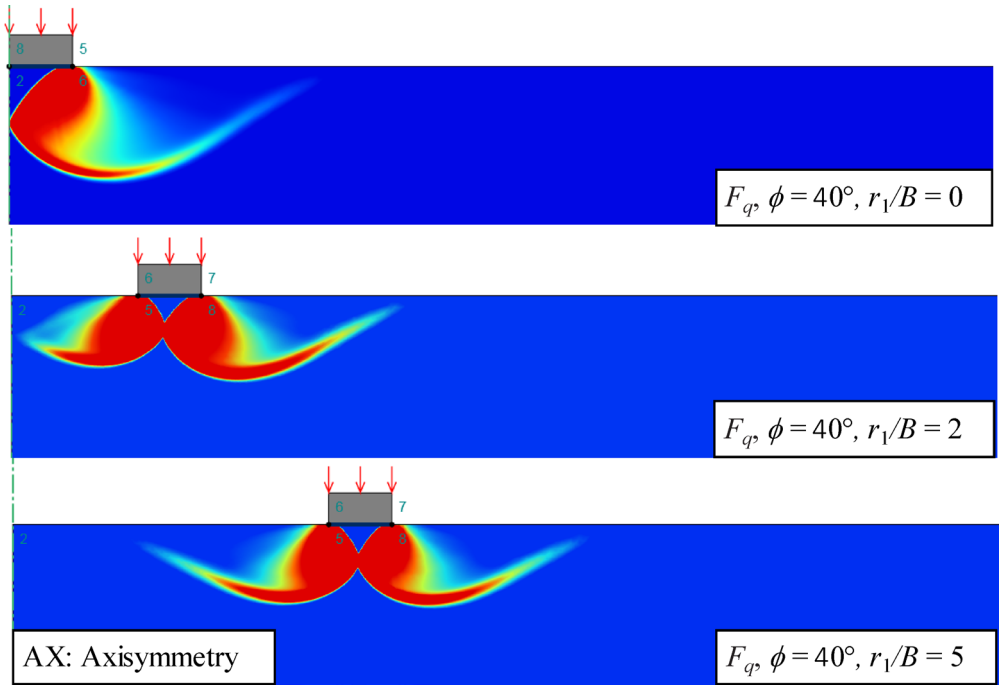

Fig. 16. Typical failure mechanisms for the analysis of F_q ($r_1/B = 0$, 2, and 5; $\phi = 40°$).

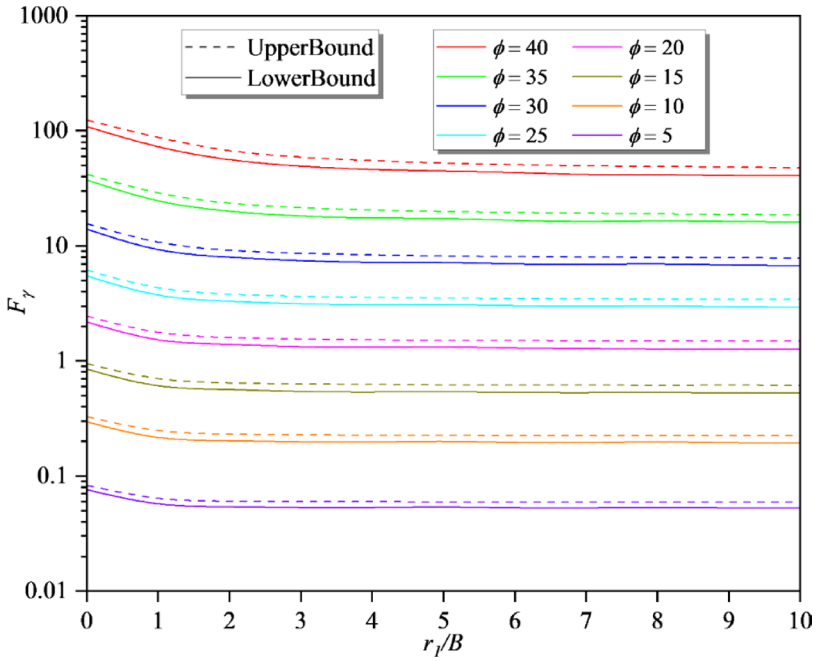

Fig. 17. The factor F_γ.

inverse relationship. This relationship is more pronounced at higher values of ϕ where F_c values increase rapidly, displaying high variability and positive skewness. This skewness suggests a right-skewed distribution of F_c with a longer tail on the higher end of the scale, particularly at higher ϕ value.

Detailed observations show that for low internal friction angles ($\phi = 0$), F_c starts from 5.989 at $r_1/B = 0$ and slightly decreases to 5.158 at $r_1/B = 10$, indicating minimal change. At moderate ϕ (20 degrees) F_c decreases from 23.328 at $r_1/B = 0$ to 15.399 at $r_1/B = 10$, showing a more noticeable decrease. For high ϕ (40 degrees), F_c reaches a maximum of 220.462 at $r_1/B = 0$ and decreases significantly to 89.139 at $r_1/B = 10$. These observations emphasize the significant impact of friction angle ϕ on the cohesion factor. Understanding these interactions is crucial for accurate modeling and prediction in geotechnical engineering applications.

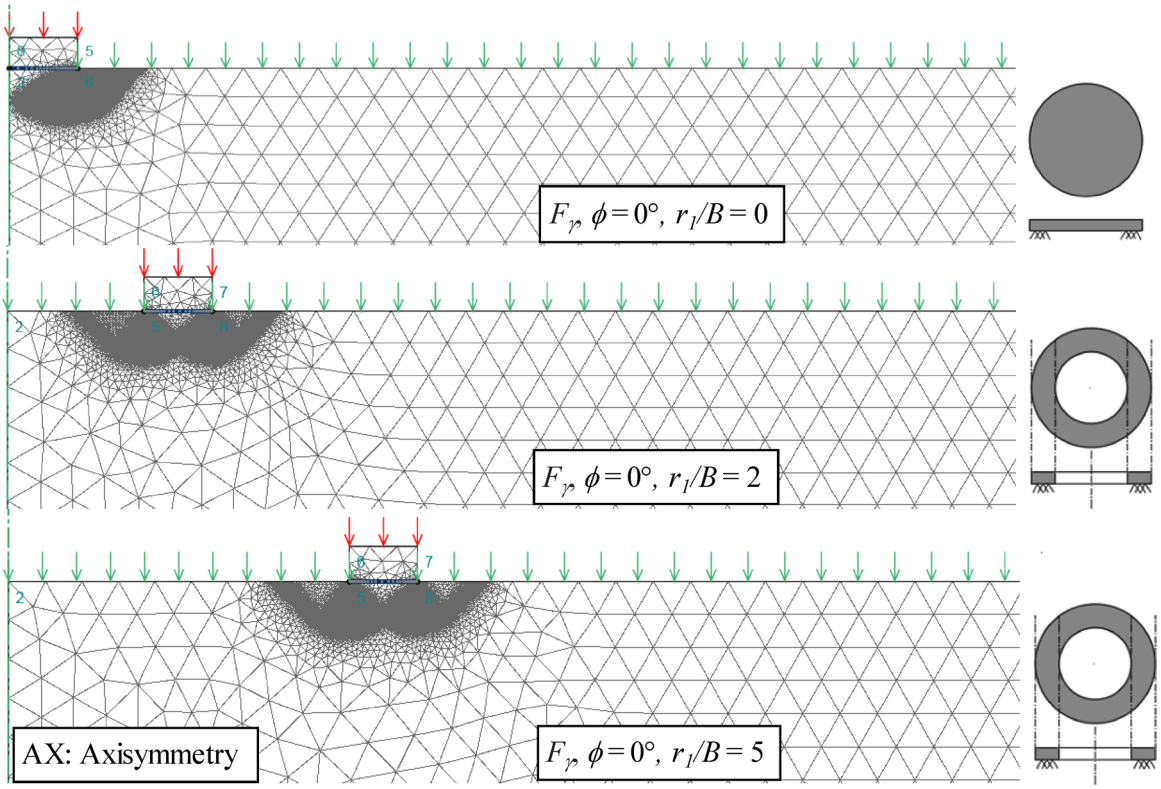

Fig. 18. Typical adaptive meshes for the analysis of F_γ ($r_1/B = 0$, 2, and 5; $\phi = 0°$).

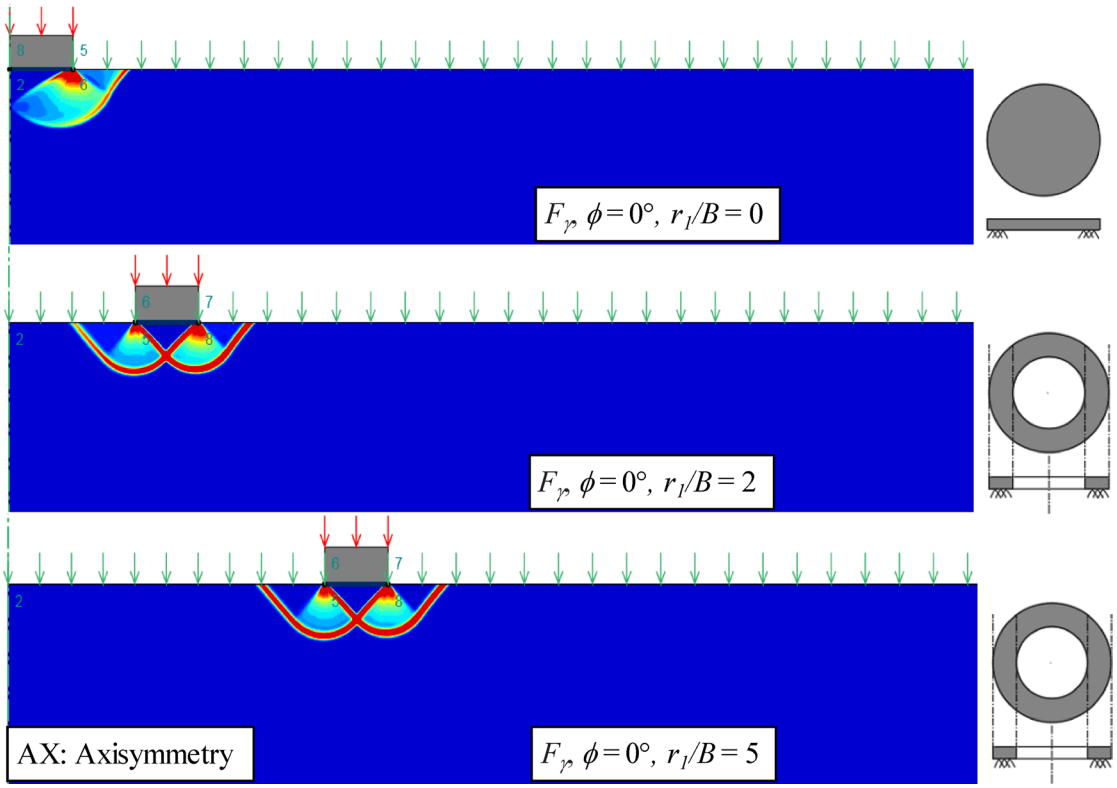

Fig. 19. Typical failure mechanisms for the analysis of F_γ ($r_1/B = 0$, 2, and 5; $\phi = 0°$).

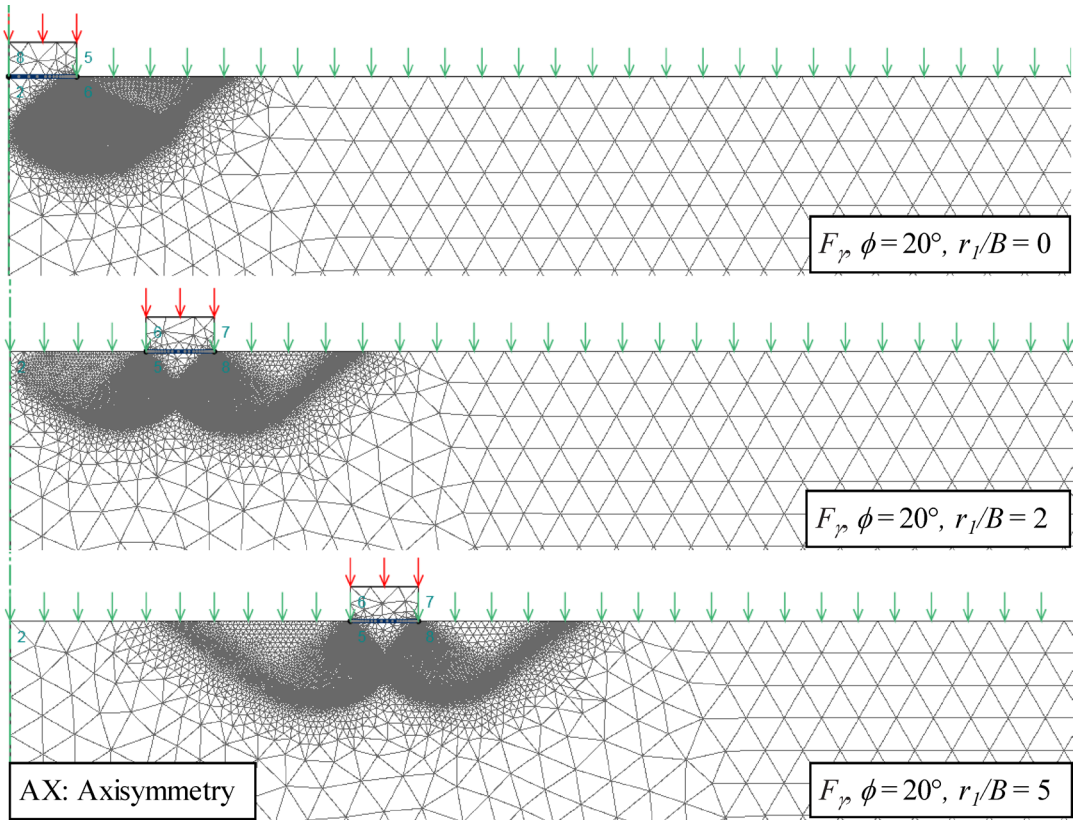

Fig. 20. Typical adaptive meshes for the analysis of F_γ ($r_1/B = 0$, 2, and 5; $\phi = 20°$).

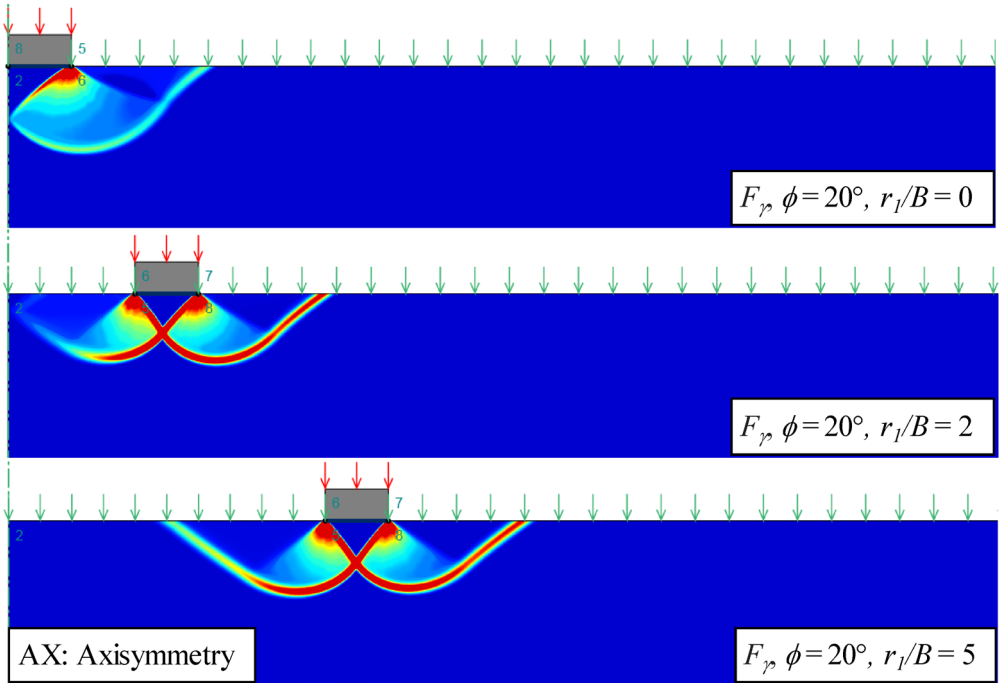

Fig. 21. Typical failure mechanisms for the analysis of F_γ ($r_1/B = 0$, 2, and 5; $\phi = 20°$).

ϕ	r_1/B	Gholami and Hosseininia[29]	Keshavarz and Kumar[13]	Kumar and Chakraborty[12]		Present Study	
		SCM	SCM	LB	UB	LB	UB
0	0	-	6.05	-	-	5.989	6.072
	1	-	5.57	-	-	5.539	5.605
	3	-	5.34	-	-	5.296	5.365
10	0	11.05	11.09	10.93	11.21	10.972	11.142
	1	10.05	9.82	6.2	6.51	9.662	9.831
	3	-	8.97	6.21	6.52	8.896	9.032
20	0	23.64	23.67	23.49	24.24	23.328	23.797
	1	21.73	20.03	11.13	11.83	19.648	20.178
	3	-	17.05	9.62	10.22	16.828	17.192
30	0	63.09	62.7	61.35	65.5	61.376	63.086
	1	55.47	53.88	25.8	28.44	51.658	53.753
	3	-	39.54	20.22	22.84	38.658	39.827

Table 1. Comparison of F_c values with previous studies.

ϕ	r_1/B	Chavda and Dodagoudar[30]	Gholami and Hosseininia[29]	Seyedi Hosseininia[2]	Present Study	
		FEM*	SCM**	FDM***	LB	UB
0	0	-	-	-	1.006	1.006
	1	-	-	-	1.006	1.006
	3	-	-	-	1.005	1.005
10	0	3.061	2.95	-	2.946	2.975
	1	2.809	2.85	-	2.713	2.745
	3	2.643	-	-	2.578	2.606
20	0	9.555	9.6	-	9.514	9.683
	1	8.2	8.91	-	8.171	8.38
	3	7.116	-	-	7.141	7.28
25	0	17.384	18.31	21	18.15	18.537
	1	14.25	16.62	17.5	15.275	15.789
	3	11.719	-	15	12.518	12.86
30	0	32	37.4	-	36.523	37.45
	1	25	33	-	30.843	32.123
	3	19.871	-	-	23.358	24.053

Table 2. Comparison of F_q values with previous studies. *Finite Element Method (FEM); **Stress Characteristic Method (SCM); ***Finite Difference Method.

ϕ	r_1/B	Keshavarz and Kumar[13]	Benmebarek et al[31]	Kumar and Chakraborty[12]		Tang and Phoon[14]	Present Study	
		SCM	FLAC	LB	UB	LB	LB	UB
20	1	2.41	2.71			2.35	2.20	2.46
	3	2.19	1.09	1.85	2.16	1.56	1.43	1.69
	5	2.41	0.6	2.32	2.6	1.41	1.32	1.55
25	1	6.07	6.78	-	-	5.9	5.51	6.16
	3	5.44	2.68	4.22	4.73	3.83	3.52	4.12
	5	5.69	1.42	5.2	5.72	3.37	3.12	3.64
30	1	15.54	17.5	-	-	15	13.99	15.68
	3	13.39	6.93	9.76	11.38	9.64	8.77	10.33
	5	13.5	3.43	10.12	11.84	7.99	7.39	8.60
40	1	124.1	133.7	-	-	117	109.18	124.01
	3	111.38	65.9	103.46	132.1	79.5	71.12	87.01
	5	107.27	26.7	80.96	114.08	53.5	48.95	58.62

Table 3. Comparison of F_γ values with previous studies.

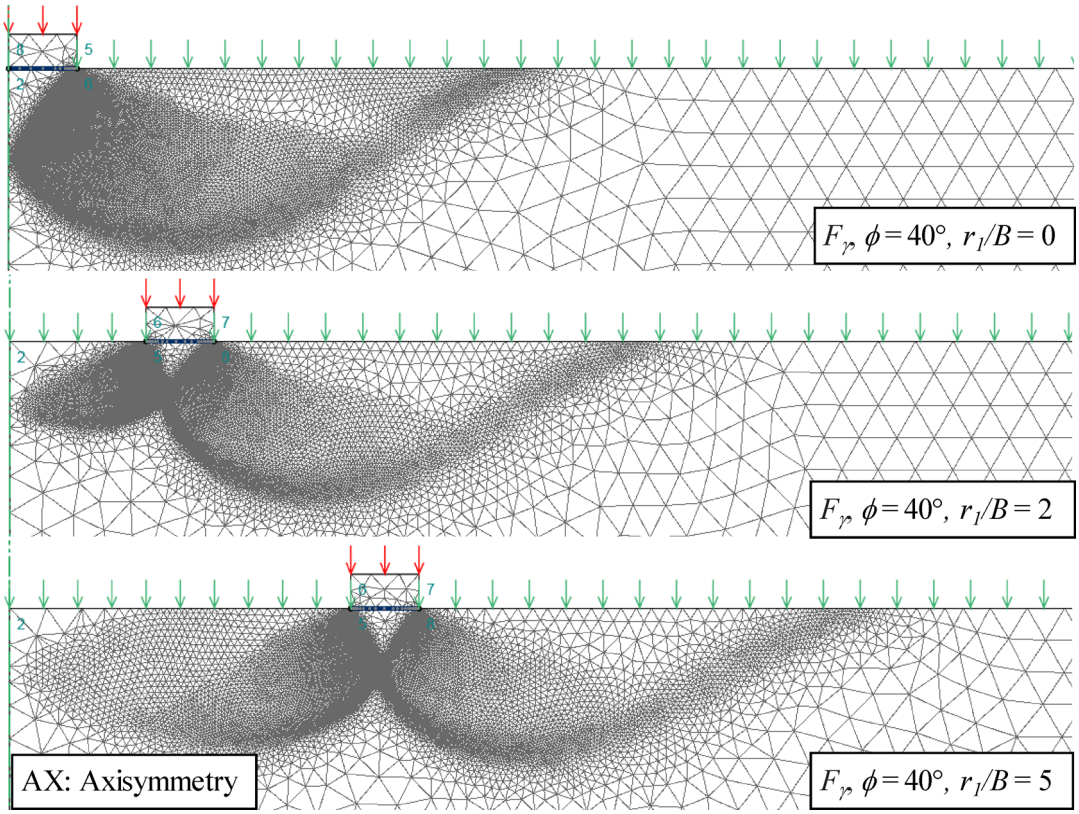

Fig. 22. Typical adaptive meshes for the analysis of F_γ ($r_1/B = 0$, 2, and 5; $\phi = 40°$).

The failure mechanism in ring footings, as demonstrated in Figs. 23, 3, 4, 5, 6 and 7, highlights the variations in F_c with the internal friction angle (ϕ) under conditions where both the unit weight (γ) and surcharge (q) are zero. This analysis provides insights into how the ratio of the inner radius to the width of the ring footing (r_1/B) influences the bearing capacity and failure patterns. Figures 23 and 3 presents adaptive meshes and contours of shear dissipation for $\phi = 0$ and three values of $r_1/B = 0$, 2, and 5, while Figs. 4 and 5 are for $\phi = 20^\circ$. For $\phi = 40^\circ$, they are shown in Figs. 6 and 7.

Depending on the internal friction angle (ϕ), the ratio of the inner radius to the width of the ring footing (r_1/B) plays a crucial role in the development of failure surfaces. Figures 23, 3, 4, 5, 6 and 7 show that, for smaller to moderate r_1/B ratios ($r_1/B < 5$), the failure mechanism shows significant interaction across the entire footing, forming a composite failure zone. For larger r_1/B ratios ($r_1/B \geq 5$), the failure mechanism in the circumferential direction under the width of the ring footing becomes isolated, indicating that the inner radius is large enough to prevent the transfer of stress and deformation between the inner and outer regions of the footing.

The failure mechanism in ring footings expands significantly with an increase in the internal friction angle (ϕ). See Figs. 3 and 5, and 7 for observations. As ϕ increases, the shear resistance of the soil also increases, leading to more pronounced failure zones. At lower values of ϕ (0° to 10°), the failure mechanism is relatively localized with shallow failure surfaces. With moderate increases in ϕ (15° to 25°), the failure mechanism becomes more defined with distinct slip lines. At higher values of ϕ (30° to 40°), the failure surfaces are well-developed and penetrate deeper into the soil mass, resulting in a broad and deep failure zone.

Surcharge factor (F_q)

Figure 8 presents the effects of the internal friction angle (ϕ) and the radius ratio (r_1/B) on the surcharge factor (F_q). Numerical results are shown for various combinations of ϕ and r_1/B, ranging from 0 to 40 degrees for ϕ and 0 to 10 for r_1/B.

A notable trend is observed in the surcharge factor (F_q) as the internal friction angle (ϕ) increases. For any given r_1/B, F_q consistently and nonlinearly increases with ϕ. For instance, at $r_1/B = 0$, F_q rises from 1.706 at $\phi = 5$ to 186.421 at $\phi = 40$. Similarly, at $r_1/B = 1$, F_q increases from 1.706 at $\phi = 5$ to 173.063 at $\phi = 40$. This pattern illustrates the strong positive correlation between ϕ and F_q that higher friction angles result in significantly higher surcharge factors.

When examining the effect of r_1/B, a clear inverse relationship is observed. For a fixed ϕ, F_q generally decreases as r_1/B increases. At $\phi = 0$, F_q remains constant at 1.006 across all values of r_1/B. However, as ϕ increases, the impact of r_1/B on F_q becomes more pronounced. For instance, at $\phi = 20$, F_q decreases from 9.514 at $r_1/B = 0$ to 6.625 at $r_1/B = 10$. At $\phi = 40$, F_q decreases from 186.421 at $r_1/B = 0$ to 75.964at $r_1/B = 10$. This decreasing trend indicates that as the ratio of the inner radius to the footing width (r_1/B) increases, the surcharge factor (F_q) diminishes, even as ϕ continues to increase.

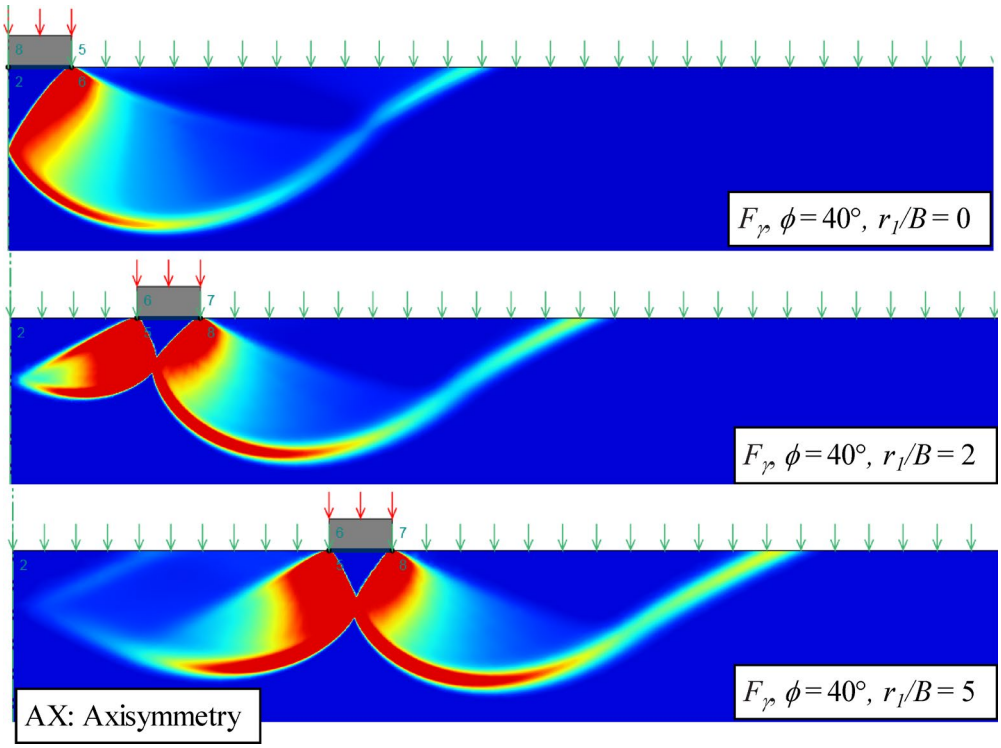

Fig. 23. Typical failure mechanisms for the analysis of F_γ ($r_1/B = 0$, 2, and 5; $\phi = 40°$).

In summary, numerical results of FELA show the significant influence of both the internal friction angle (ϕ) and the ratio of the inner radius to the width of the ring footing (r_1/B) on the surcharge factor (F_q). The surcharge factor increases with ϕ, while it decreases as r_1/B increases, emphasizing the interaction among these variables in establishing the surcharge factor for ring footings.

The resulting failure mechanisms of F_q analyses are presented in Figs. 9, 10, 11, 12, 13 and 14 for ($\phi = 0°$, 20°, and 40°; $r_1/B = 0$, 2, and 5). In all F_q analyses, both the unit weight (ϕ) and unit cohesion (c) are set as zero as discussed before. Results show that as the internal friction angle (ϕ) increases, the shear resistance of the soil increases, leading to more pronounced failure zones. At lower values of ϕ (0° to 10°), the failure mechanism is localized with shallow surfaces. As ϕ increases to moderate levels (15° to 25°), the failure mechanism becomes more defined with distinct slip lines. At higher ϕ values (30° to 40°), the failure surfaces penetrate deeper into the soil mass, creating a broad and deep failure zone.

Note that the radius ratio (r_1/B) significantly influences the failure mechanism at higher ϕ values (see Figs. 13 and 14). For r_1/B ratios less than 5, the failure mechanism interacts across the entire footing, forming a composite failure zone. For r_1/B ratios of 5 or more, the failure mechanism in the circumferential direction under the width of the ring footing becomes isolated, indicating minimal stress and deformation transfer between the inner and outer regions.

Unit weight factor (F_γ)

The effects of the internal friction angle (ϕ) and the inner radius ratio (r_1/B) on the unit weight factor (F_γ) are shown in Fig. 15. Numerical results of F_γ values are selected for various combinations of ϕ and r_1/B, ranging from 0 to 40 degrees for ϕ and 0 to 10 for r_1/B.

A notable trend is observed in the unit weight factor (F_γ) as the internal friction angle (ϕ) increases. For any given r_1/B, F_γ consistently increases with ϕ. For instance, at $r_1/B = 0$, F_γ rises from 0.077 at $\phi = 5$ to 109.18185 at $\phi = 40$. Similarly, at $r_1/B = 1$, F_γ increases from 0.077 at $\phi = 5$ to 71.123 at $\phi = 40$. This pattern illustrates the strong positive correlation between ϕ and F_γ, indicating that higher friction angles result in significantly higher F_γ factors.

When examining the effect of r_1/B, a clear inverse relationship is observed. For a fixed ϕ, F_γ generally decreases as r_1/B increases. At $\phi = 0$, F_γ remains constant at approximately 0.00025 across all values of r_1/B. However, as ϕ increases, the impact of r_1/B on F_γ becomes more pronounced. For instance, at $\phi = 20$, F_γ decreases from 2.195 at $r_1/B = 0$ to 1.263 at $r_1/B = 10$. At $\phi = 40$, F_γ decreases from 109.182 at $r_1/B = 0$ to 40.888 at $r_1/B = 10$. This decreasing trend indicates that as the ratio of the inner radius (r_1/B) increases, the unit weight factor (F_γ) diminishes, even as ϕ continues to increase.

The failure mechanisms depicted in Figs. 16, 17, 18, 19, 20 and 21 demonstrate the impact of the friction angle (ϕ) and the relative cavity distance (r_1/B) on system stability. At low friction angles, such as zero degrees (Figs. 16 and 17), the failure zones are compact and localized around the footing and cavity, with cohesion dominating the response. As the friction angle increases to twenty and forty degrees (Figs. 18, 19, 20 and 21),

the failure mechanisms expand significantly, showing larger slip surfaces and an increasing influence of friction. The interaction between the foundation load and the cavity becomes more evident, especially at higher friction angles, resulting in broader deformation zones.

The position of the cavity relative to the footing also significantly influences the failure patterns. When the cavity is directly beneath the footing, corresponding to a cavity distance ratio of zero, it causes highly localized failure with intense stress concentrations (Figs. 16 and 18, and 20). When the cavity is laterally offset, with a cavity distance ratio of two, asymmetric failure zones are observed (Figs. 17 and 19, and 21). At a cavity distance ratio of five, the cavity has minimal impact, and the failure zones exhibit symmetrical patterns. The adaptive meshing (Figs. 16 and 18, and 20) effectively captures critical stress and deformation zones, ensuring detailed identification of slip surfaces. These results emphasize the combined role of soil properties and cavity positioning in foundation stability, providing practical insights for safe design.

Summary

The above numerical results of bearing capacity stability factors (F_c, F_q, and F_γ) highlight the significant influence of both the internal friction angle (ϕ) and the ratio of the inner radius to the width of the ring footing (r_1/B) on the three factors. Additionally, understanding the failure mechanism in ring footings under various ϕ and r_1/B ratios has significant implications for geotechnical design and analysis. By selecting appropriate values of ϕ and r_1/B, engineers can optimize the design of ring footings to achieve desired stability and bearing capacity. For instance, larger r_1/B ratios can be used to isolate failure zones, enhancing the footing's performance in specific applications. The detailed failure mechanisms observed can be used to develop more accurate predictive models for bearing capacity and failure behavior in ring footings, incorporating the effects of ϕ and r_1/B to provide reliable predictions for various soil conditions. Furthermore, by understanding how ϕ and r_1/B influence failure mechanisms, safety margins can be improved in the design process, ensuring that the footings perform reliably under different loading conditions and soil characteristics.

Comparative analysis with existing literature

Although the FELA method includes built-in error indicators for upper and lower bounds, it is prudent to conduct a thorough comparison with previously published results. This comparative analysis enhances confidence in the applicability of the three factors. The comparisons of bearing capacity stability factors (F_c, F_q, and F_γ) with previous studies are presented in Tables 1, 2 and 3, respectively.

For the factor F_c, the numerical results in Table 1 show consistent agreement between the present study and other studies. The UB and LB results from the present study are close to stress characteristic method (SCM) of Keshavarz and Kumar[13]; Gholami and Hosseininia[29]. Noting the big differences in Kumar and Chakraborty[12] for $r_1/B = 2$ and 3, the reasons may be attributed to the relatively coarse meshes (2320–2400 triangular elements) as well as the lack of adaptive meshing technique used in the present study.

For the factor F_q, the numerical results in Table 2 demonstrate consistent agreement between the present study and other research. The UB and LB results from this study closely match the FEM results of Chavda and Dodagoudar[30], the SCM results of Gholami and Hosseininia[29], and the FDM results of Hosseininia[2], except in cases with larger soil friction angles and r_1/B. The built-in error between UB and LB is also excellent for achieving the factor F_q, further demonstrating the robustness of the current adaptive meshing technique.

For the factor F_γ, the present values are compared with (1) the slip-line solutions obtained by Keshavarz and Kumar[13], (2) the numerical results of Benmebarek et al.[31] using the finite-difference software FLAC, (3) the limit analysis for upper bound and lower bound solutions of Kumar and Chakraborty[12], and (4) the lower bound limit analysis of Tang and Phoon[14]. The numerical results in Table 3 demonstrate inconsistent agreement between the present study and other research, with more discrepancies than those previously observed for F_c and F_q in Tables 1 and 2.

Noting that our UB and LB can bracket the true solutions ranging from 1% ($\phi = 0^\circ$) to 15% ($\phi = 40^\circ$), these rigorous F_γ values are considerably lower than the SCM method of Keshavarz and Kumar[13]. The reported values from Benmebarek et al.[31], Kumar and Chakraborty[12] show the greatest discrepancies among others. Nevertheless, the results reported by Tang and Phoon[14] are in good agreement with our UB and LB solutions. As stated in Tang and Phoon[14], the solution accuracy very much depends on the choice of failure mechanisms, boundary conditions as well as the meshing refinement with adaptively meshing technique. Indeed, this is especially important for large values of soil friction angle and r_1/B. This alignment ensures the robustness and credibility of our F_γ values. The close correlation between our findings and previous research provides valuable confirmation of the accuracy and reliability of our analysis.

Soft computing model

Dataset and statistical descriptions

Table 4 provides a comprehensive statistical overview of the input and output variables. The input variables, specifically the ratio of inner radius to the footing width (r_1/B) and the internal friction angle (ϕ), display symmetrical distributions. The mean values for r_1/B and ϕ are 5 and 20, respectively, with standard deviations of 3.1623 and 12.9099, indicating moderate to high variability. The skewness values for both variables are 0.0000, reflecting perfectly symmetrical distributions, suggesting a balanced spread of values around the mean. The histogram of these input variables, shown in Fig. 24, illustrates this symmetrical distribution, reinforcing the uniformity in their data spread.

In contrast, the output variables (F_c, F_q, and F_γ) show significant variability and positive skewness, indicating the presence of extreme values. F_c has a mean value of 16.037, but its standard deviation of 40.6936 and skewness of 2.3271 indicate a wide range of values with a heavy tail on the higher end. Similarly, F_q and F_γ have mean

Variables	Unit	Notation	Min	Mean	Std	Skewness	Max
r_1/B	-	X_1	0	5	3.1623	0.0000	10.000
Internal friction angle (ϕ)	degree	X_2	0	20	12.9099	0.0000	40.000
Cohesion factor, F_c	-	*Y1*	5.158	16.037	40.6936	2.3271	220.462
Surcharge factor, F_q	-	*Y2*	1.005	6.853	35.3550	2.4730	186.421
Unit weight factor, F_γ	-	*Y3*	0.000	1.305	17.8862	2.8582	109.182

Table 4. The statistical description of the input and output variables.

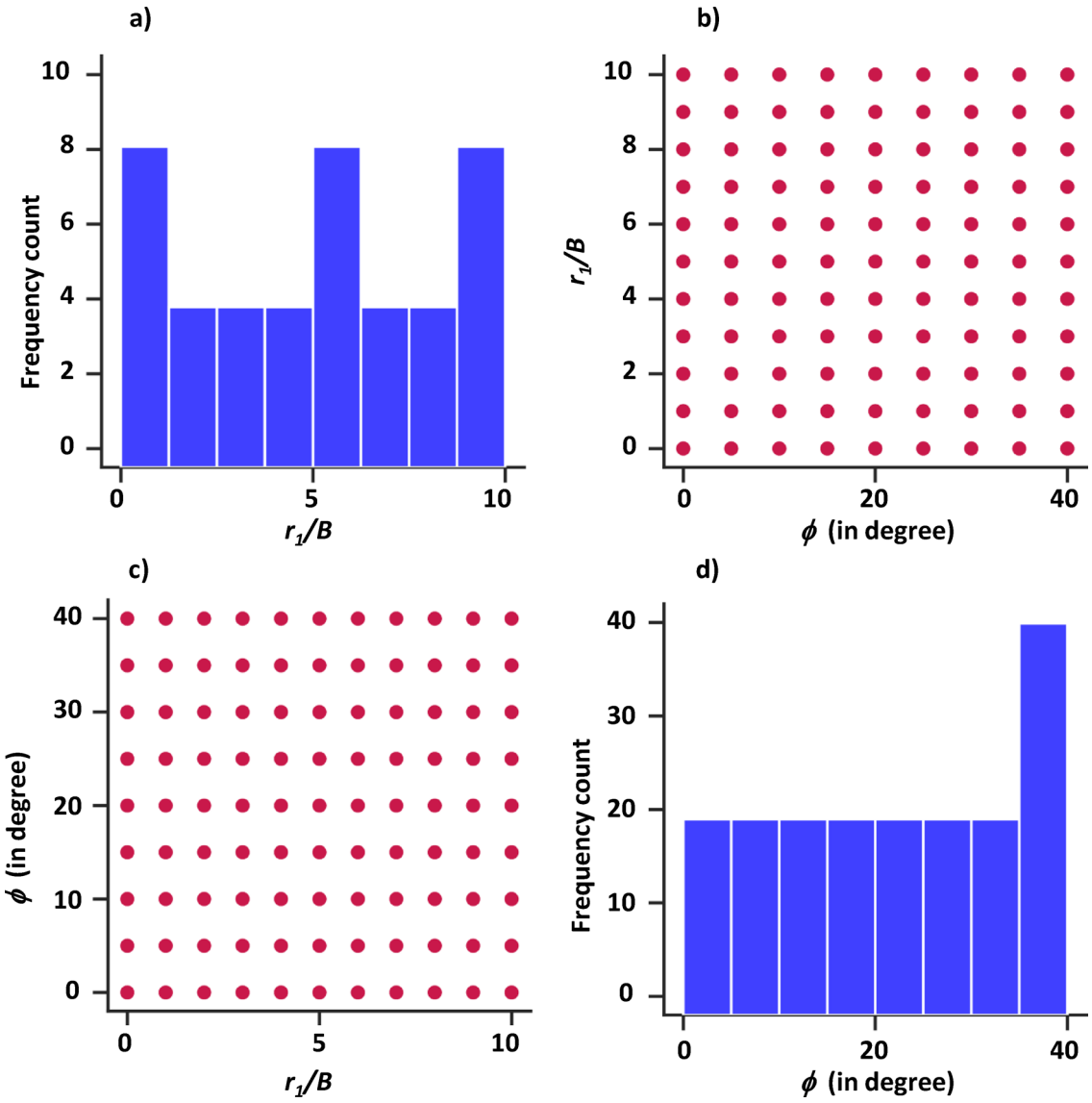

Fig. 24. (**a**) Histogram of frequency count versus the ratio of the inner radius to the width of the ring footing (r_1/B); (**b**) Contour plot of r_1/B against the internal friction angle (ϕ) in degrees; (**c**) Heatmap of the internal friction angle (ϕ) in degrees against r_1/B; (**d**) Histogram of frequency count versus the internal friction angle (ϕ) in degrees.

values of 6.853 and 1.305, respectively, but their standard deviations (35.3550 and 17.8862) and skewness values (2.4730 and 2.8582) reveal distributions heavily influenced by high outliers. These skewness values suggest that while most observations are clustered towards the lower end, a few high values significantly impact the mean, reflecting the complex and varied nature of soil properties and their influence on bearing capacity. The histograms for these output variables, shown in Fig. 25, illustrate this statistical variability and skewness. Such

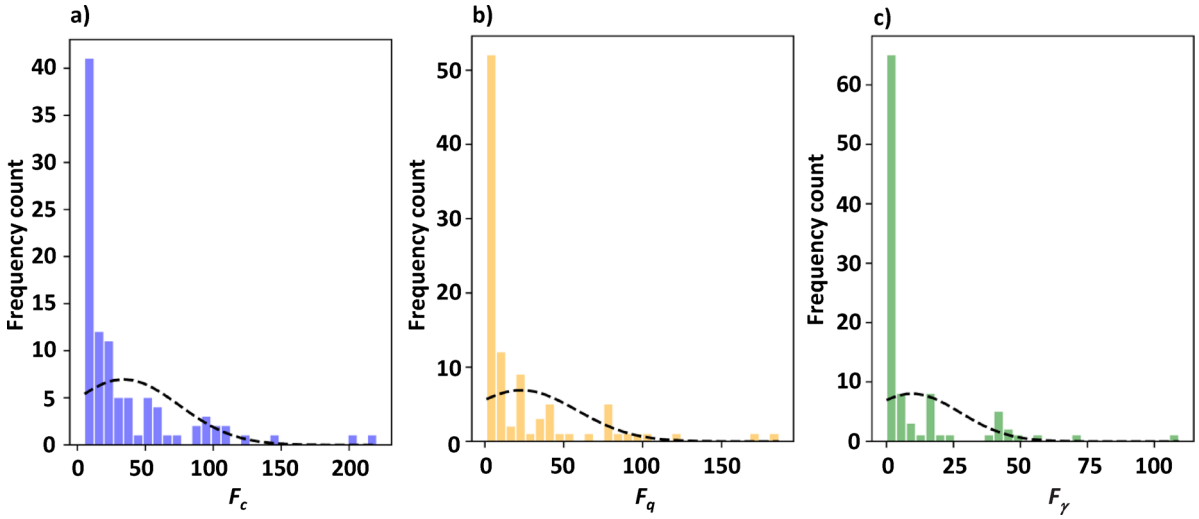

Fig. 25. Visualization of dataset in histograms: (**a**) F_c; (**b**) F_q; (**c**) F_γ.

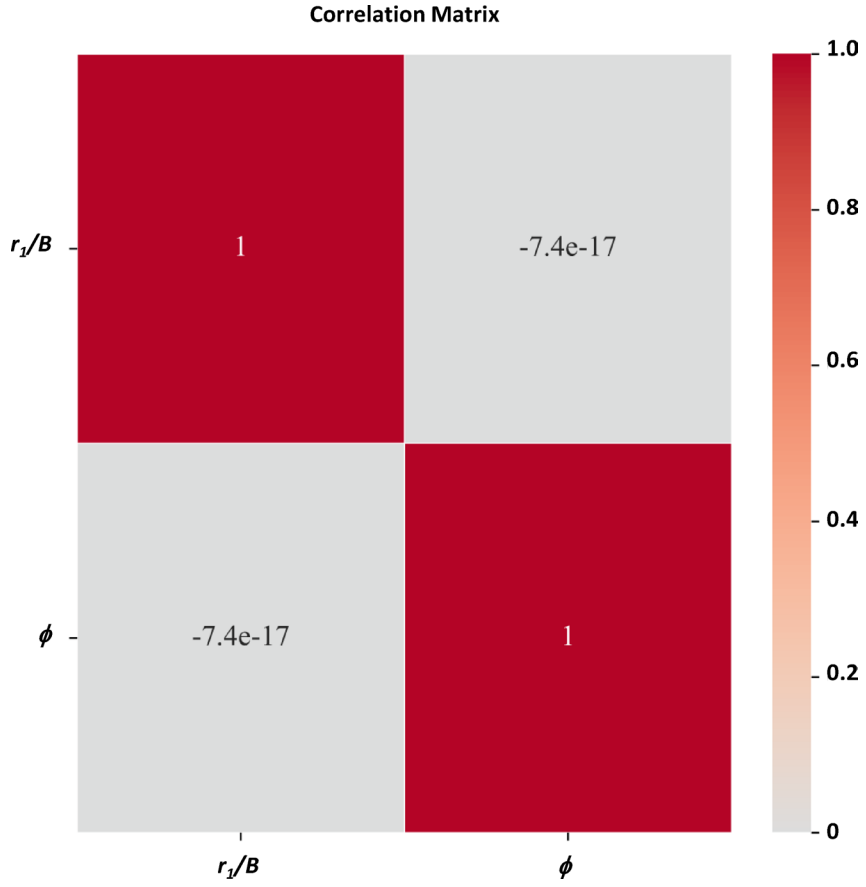

Fig. 26. Correlation matrix.

characteristics emphasize the need for advanced predictive models, like Kolmogorov-Arnold Networks, to effectively capture complex relationships and accurately assess bearing capacities in geotechnical applications.

The heatmap of the correlation matrix shown in Fig. 26 indicates that the variables r_1/B and ϕ (internal friction angle) are uncorrelated. This means that variations in r_1/B do not predict changes in ϕ and vice versa. The absence of correlation suggests that there is no linear relationship between these two variables, and their interactions may not be effectively captured by simple correlation analysis alone. This lack of correlation

implies that other methods or models may be necessary to explore and understand any potential non-linear dependencies or complex interactions between r_1/B and ϕ.

Accordingly, a Kolmogorov–Arnold Network (KAN) is adopted in this study to address these nonlinearities. Unlike conventional Artificial Neural Networks (ANNs) that rely on fixed activation functions and dense transformations, KAN employs *learnable spline-based functional connections* that adapt their shape to the underlying data structure. This flexibility enables KAN to efficiently capture the coupled nonlinear behavior between r_1/B and ϕ that governs the stability factors (F_c, F_q, F_γ), achieving high predictive accuracy with fewer parameters. In addition, the explicit functional form of each spline provides transparent insight into the contribution of individual inputs, thereby bridging data-driven modeling with physical interpretation.

Kolmogorov-Arnold networks (KAN)

The mathematical foundation of KAN has been extensively detailed by Liu et al. (2024). This study will provide a concise overview of the key aspects of KAN's theory.

KAN's theorem posits that any continuous multivariate function, within a bounded domain, can be represented as a composition of continuous, single-variable functions and addition operations. A smooth function ($f : \mathbb{R}^n \to \mathbb{R}$) can be written as:

$$f(x) = f(x_1, ..., x_n) = \sum_{q=1}^{2n+1} \Phi_q \left(\sum_{p=1}^{n} \varphi_{q,p}(x_p) \right), \tag{2}$$

where ($\varphi_{q,p} : \mathbb{R} \to \mathbb{R}$) and ($\Phi_q : \mathbb{R} \to \mathbb{R}$). They showed that addition is the only true multivariate function, as others can be written using univariate functions and sums. While this initially seemed beneficial for machine learning, the non-smooth and fractal nature of these 1D functions made them impractical to learn, rendering the Kolmogorov-Arnold theorem seemingly useless.

By extending networks to arbitrary widths and depths, we can overcome these limitations. Most real-world functions are smooth and sparse, making Kolmogorov-Arnold representations feasible. This approach, similar to the perspective of physicists who focus on typical cases, ensures the applicability and generalizability of physics and machine learning. The Kolmogorov-Arnold theorem provides a framework for approximating complex functions by breaking them down into simpler, univariate components.

The structure of a Kolmogorov-Arnold Network (KAN) can be understood through the concept of a 'KAN layer'. This layer consists of a matrix of 1D functions, denoted as (Φ), where each function ($\varphi_{q,p}$) possesses trainable parameters. The original Kolmogorov-Arnold representation, typically a two-layer structure denoted as($[n,\ 2n+1,\ 1]$), utilizes:

- An inner layer that maps (n)-dimensional inputs to a $(2n+1)$-dimensional hidden layer.
- An outer layer that maps this hidden layer to a single output.

Deeper KANs are constructed by stacking multiple KAN layers, similar to Multi-Layer Perceptrons (MLPs), which enhances representational power and allows modeling of more complex functions. A key advantage of using splines to parameterize the activation functions in KANs is the ability to perform grid extension. This technique increases the resolution of the spline grid(G), improving accuracy without retraining the entire network. This incremental enhancement through grid refinement contrasts with the rigid and computationally expensive scaling methods of MLPs. The process involves:

- Initializing the parameters of the finer grid using those of the coarser grid.
- Minimizing the distance between the two representations.

The order of the spline used to parameterize activation functions in KANs is a critical factor influencing their approximation capabilities. B-splines of order (k), where (k) denotes the polynomial degree, are commonly employed. Higher spline orders enhance the smoothness and expressiveness of activation functions, enabling more accurate approximation of complex functions.

Theorem establishes that for functions representable by $(k+1)$ times continuously differentiable compositions, a KAN with B-spline activations of order (k) achieves approximation errors that decrease as the grid size $(G)$is refined. Specifically, the root mean squared error (RMSE) loss (ℓ) scales with the number of model parameters (N) as$(\ell \propto N^{-(k+1)})$. This implies that higher spline orders facilitate faster convergence with fewer parameters for smoother functions. Choosing the spline order involves a trade-off between approximation accuracy and computational cost. While higher orders improve approximation quality, they increase the parameter count, potentially affecting training efficiency and resource requirements.

KANs offer several advantages for machine learning, including the ability to model complex functions with greater accuracy and incremental accuracy enhancement through grid refinement without the need for full network retraining. Additionally, KANs align with the physicists' focus on typical cases, ensuring practical applicability and generalizability.

Figure 27 presents a schematic representation of the symbolic regression process using KAN to predict the bearing capacity of ring footing. This figure encapsulates the methodology and the intricate relationship between input parameters and the bearing capacity factors. Symbolic regression via KAN involves identifying and formulating the underlying mathematical expressions that describe the complex interactions within the dataset. It also demonstrates the capability to handle nonlinear and complex relationships between the geometric parameters of the ring footing (such as the ratio of internal radius to thickness, r_1/B) and soil properties (including

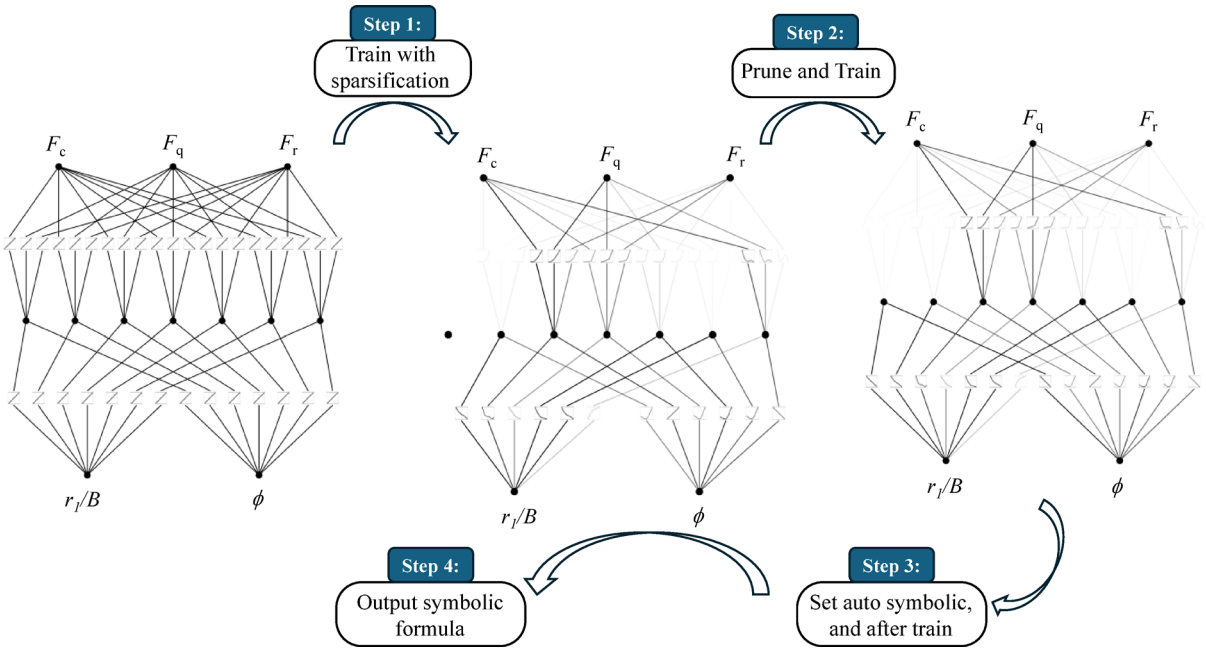

Fig. 27. Schematic of symbolic regression with KAN for predicting the bearing capacity of ring footing.

Network type	Kolmogorov-Arnold Networks
Number of neurons in the input layer	2
Number of middle layer	1
Width N in the middle layer	7
Number of nodes in the output layer	3
Number of grid points	3
Spline of order k	3
Optimizer	Limited-memory BFGS (L-BFGS) optimizer
Loss function	RMSE
Epoch	70

Table 5. Details of tuned KAN topology.

the internal friction angle, ϕ). The figure also illustrates how KAN is used to develop robust predictive models for the bearing capacity factors (F_c, F_q, and F_γ).

The process begins with the input parameters, progresses through the hidden layers of the KAN, and culminates in the output, which predicts the bearing capacity factors. The diagram highlights the efficiency of KAN in capturing the essential features of the data, ensuring high accuracy and reliability in predictions. Overall, Fig. 27 not only demonstrates the technical process of symbolic regression with KAN but also emphasizes the methodological advancements and practical implications of this novel approach in predicting the bearing capacity of ring footings on frictional–cohesive soils.

Building upon this conceptual framework, the specific implementation details of the KAN—such as the network architecture, spline parameters, grid resolution, and optimized hyperparameters—were systematically determined to achieve the best trade-off between model complexity and predictive accuracy. These details, along with comparative results against the benchmark ANN model, are presented and discussed in Sect. 5.3 (Results and Discussions) and summarized in Table 5. This transition from theoretical formulation to empirical evaluation reinforces the methodological consistency and transparency of the proposed framework.

Results and discussion

Optimizing topology

The performance of KANs is affected by the choice of several hyperparameters. This section examines the impact of the number of grid point, middle layers and the spline order on model performance.

The number of grid points used to define the spline functions within the KAN architecture is crucial for determining model accuracy. Increasing the number of grid points allows for a more fine-grained and flexible representation of the underlying function. This fine-graining process can significantly improve the model's ability to capture complex and nuanced relationships in the data, leading to lower training and test errors. Experiments

demonstrate that KANs can achieve faster scaling laws compared to conventional MLPs, highlighting their efficiency in representing functions with increasing complexity. As the grid becomes finer, the KAN's ability to approximate the target function improves, resulting in a decrease in test MSE that often follows a power law relationship with the number of grid points. This relationship is depicted in Fig. 28a, where the test MSE decreases as the number of grid points increases. However, an excessively fine grid can lead to overfitting, where the model learns the training data too well and performs poorly on unseen examples. Therefore, it is essential to find a balance in the number of grid points to optimize model performance without overfitting. In this task, the chosen number of 3 grid points provides a balance that enhances model accuracy while avoiding the pitfalls of overfitting.

The number of nodes in the middle layers of a KAN dictates the network's width and significantly impacts its capacity to learn complex representations. Wider KANs, with more nodes in their middle layers, are capable of learning more intricate functions. The Kolmogorov-Arnold representation theorem suggests a specific width of $(2n+1)$ for a two-layer network with input dimension n. However, practical applications often necessitate wider and deeper networks. Figure 28b illustrates the relationship between the number of nodes in the middle layers and the model's performance. As the number of nodes increases, the network's ability to capture complex relationships improves, leading to a decrease in training and test errors. This enhanced capability allows KANs to achieve more accurate approximations of the target functions. However, there is a trade-off to consider. While wider networks have greater expressive power, they also risk overfitting and require increased computational resources. The optimal width of KANs balances these factors, maximizing performance while managing overfitting and computational demands.

The spline order determines the smoothness and differentiability of the activation functions within the KAN. Higher-order splines offer smoother approximations but may increase computational complexity. Figure 28c illustrates the impact of different spline orders on model performance. Higher-order splines enhance

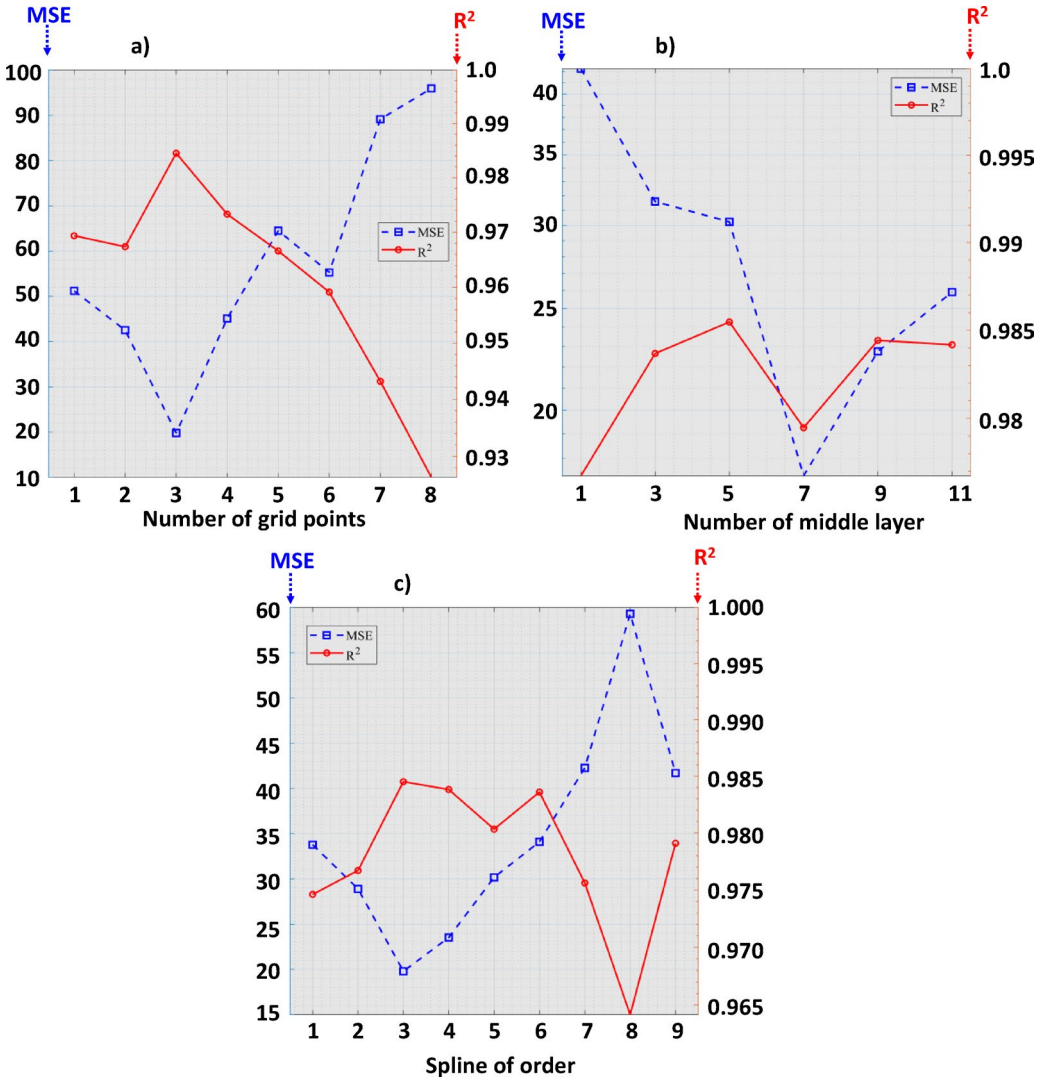

Fig. 28. Model performance across different numbers of: (**a**) grid points; (**b**) nodes in the middle layer; and (**c**) spline order.

the smoothness and expressiveness of the activation functions, allowing the KAN to capture more nuanced relationships in the data. This improvement can lead to lower training and test errors, as depicted in the figures. However, the increased computational burden and overfitting associated with higher spline orders must be carefully managed. The trade-off between accuracy and computational cost is a key consideration when selecting the appropriate spline order. While the spline order significantly affects the model's performance, its impact on the interpretability of KANs is relatively subtle compared to other hyperparameters such as the number of grid points or nodes.

The choice of optimizer significantly impacts the performance and convergence behavior of machine learning models. In this study, we compare the performance of the Limited-memory BFGS (L-BFGS) optimizer with the Adam optimizer. Figure 29 illustrates the training histories of Kolmogorov-Arnold Networks optimized with Limited-memory BFGS (L-BFGS) and Adam. The comparison reveals that L-BFGS outperforms Adam in terms of convergence speed and final error reduction. The training process is divided into three distinct steps, each aimed at enhancing model efficiency and mitigating overfitting. Step 1, Train with Sparsification (Epochs 0–10): during the initial phase of training (Epochs 0 to 10), the model is trained with sparsification techniques. This step involves introducing sparsity in the network's parameters. The figure shows that both optimizers perform similarly during this phase. Sparsification helps in setting up a baseline model by enforcing structure and reducing the initial complexity of the network. Step 2, Prune and Train (Epochs 10–20): the training process includes pruning, which involves removing less significant connections from the network. This step further simplifies the model by eliminating redundant parameters, helping to focus the network's capacity on the most important features. After pruning, the model is retrained to adjust to the reduced structure. Step 3, Train Affine Parameters (Epochs 20–70): in the final training phase, the focus shifts to optimizing affine parameters while keeping the pruned network structure intact. This step refines the remaining parameters to improve model accuracy and generalization. The results show that L-BFGS continues to outperform Adam in this phase, achieving lower training and validation errors. The effectiveness of L-BFGS in this stage highlights its ability to efficiently optimize the model's affine parameters, leading to better overall performance.

The model topologies have been optimized, as summarized in Table 5. The combination of these carefully chosen parameters ensures that the KANs are both efficient and precise in predicting the stability factors. The single middle layer with a moderate width, coupled with a sufficient number of grid points and cubic splines, strikes a balance between complexity and generalization ability. The use of the L-BFGS optimizer further enhances the model's performance by ensuring fast and reliable convergence during training. By fine-tuning these hyperparameters, the optimized KAN configurations achieve high predictive accuracy, demonstrating their effectiveness in modeling the stability factors with a high degree of precision.

Furthermore, we compare Kolmogorov-Arnold Networks (KANs) with a densely connected artificial neural network (ANN) using a single hidden layer of 50 neurons. This is shown in Table 6. Note that KANs often require significantly fewer parameters to achieve comparable or superior accuracy compared to dense ANNs. This efficiency is due to KANs' ability to represent complex functions using fewer, adaptable splines. The densely connected ANN, with its larger number of parameters, may not perform as well as the smaller KAN. This suggests that KANs offer a more efficient parameterization for representing complex functions. While traditional MLPs use fixed activation functions, the learnable activations in KANs provide additional flexibility and efficiency.

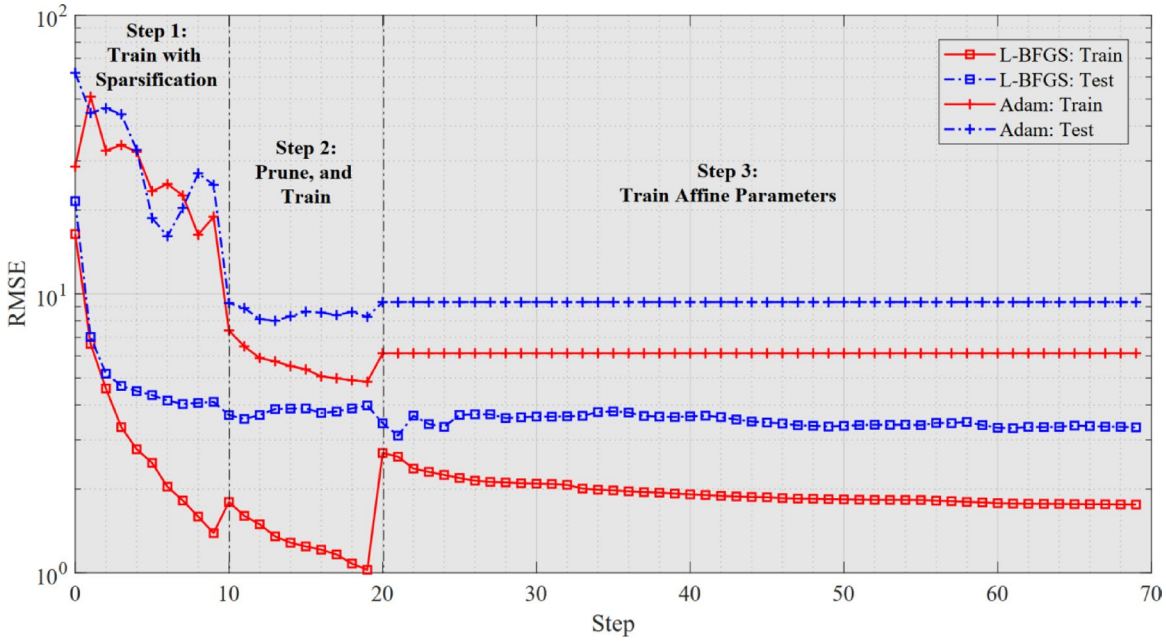

Fig. 29. Comparison of training histories for L-BFGS and Adam optimizers.

Network type	Neural Networks
Number of neurons in the input layer	2
Number of neurons in the hidden layer	50
Number of neurons in the output layer	3
Loss function	MSE
Epoch	500

Table 6. Details of ANN topology.

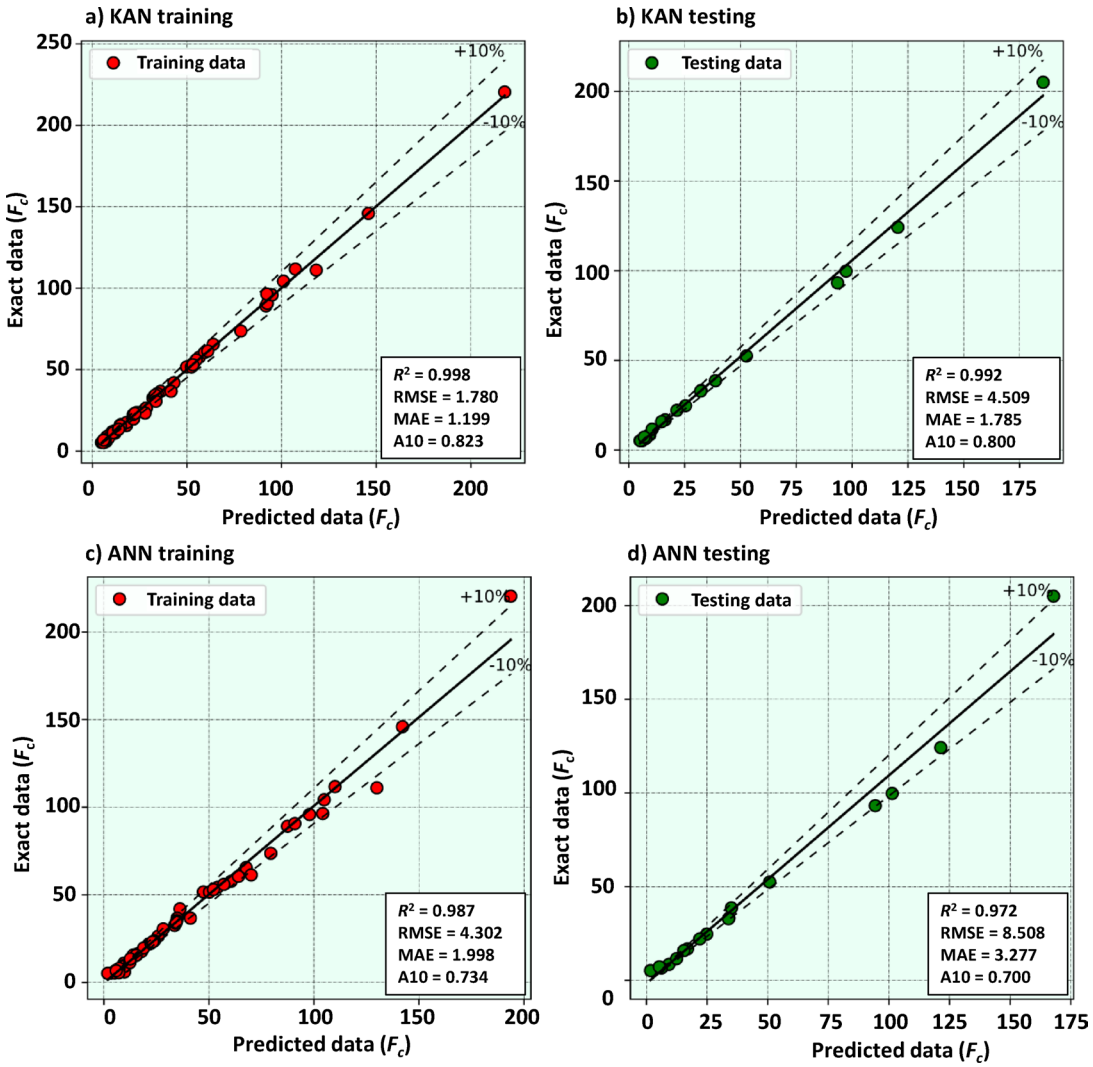

Fig. 30. Regression plots for F_c: (**a**) KAN with training data; (**b**) KAN with testing data; (**c**) ANN with training data; (**d**) ANN with testing data.

Assessing performance

Figure 30 presents the regression plots for predicting the bearing capacity factor (F_c) using Kolmogorov-Arnold Networks (KAN) and Artificial Neural Networks (ANN) on both training and testing datasets. The KAN model demonstrates remarkable predictive accuracy with an R^2 value of 0.998 for the training data and 0.992 for the testing data, indicating that it explains 99.8% and 99.2% of the variance, respectively. These high R^2 values highlight KAN's superior capability in capturing the underlying patterns within the data. Furthermore, the KAN model exhibits significantly lower Root Mean Square Error (RMSE) and Mean Absolute Error (MAE) values. They are 1.78 and 1.199 for training, and 4.509 and 1.785 for testing, as compared to ANN, suggesting minimal prediction deviations and high reliability. The Accuracy within 10% (A10) metric for KAN stands at 0.823 for training and 0.800 for testing, indicating that 82.3% and 80% of predictions are within 10% of the actual values,

respectively. This strong performance underscores KAN's superior predictive capability for F_c and demonstrates its efficiency in representing nonlinear dependencies with fewer parameters than ANN.

Figure 31 illustrates the regression plots for the bearing capacity factor (F_q) predicted by KAN and ANN. For the KAN model, the R^2 values are 0.994 for training and 0.993 for testing, signifying its high efficacy in capturing the variance in both datasets. The model's RMSE and MAE values are 2.452 and 1.714 for training, and 3.78 and 2.082 for testing. They are lower than those of the ANN model, indicating reduced prediction errors. Although the A10 metric for KAN is 0.392 for training and 0.500 for testing, which is lower compared to ANN's values, it still demonstrates a significant proportion of predictions within a 10% margin of error. The consistent performance of KAN across both datasets highlights its effectiveness and reliability in modeling F_q, despite the slightly lower A10 metric.

Figure 32 shows the regression plots of the bearing capacity factor (F_γ) using KAN and ANN. The ANN model exhibits outstanding performance with an R^2 of 0.999 for testing data, suggesting near-perfect predictive accuracy. The model achieves remarkably low RMSE and MAE values of 0.716 and 0.599, respectively, reflecting minimal prediction errors. The A10 metric for ANN is 0.400, indicating that 40% of predictions fall within 10% of the actual values. In contrast, the KAN model shows good performance with a R^2 value of 0.977 for training and 0.966 for testing. However, it has higher RMSE and MAE values: 2.618 and 1.448 for training, and 3.758 and 1.857 for testing, as compared to ANN. The A10 metric for KAN is lower at 0.177 for training and 0.300 for testing, suggesting a smaller proportion of predictions within the 10% margin.

In summary, the regression analyses across Figs. 30 and 31, and 32 reveal the robustness and precision of the KAN model in predicting the three bearing capacity factors. KAN consistently achieves higher R^2 values and lower error metrics for F_c and F_q than ANN, whereas ANN slightly outperforms KAN for F_γ. Overall,

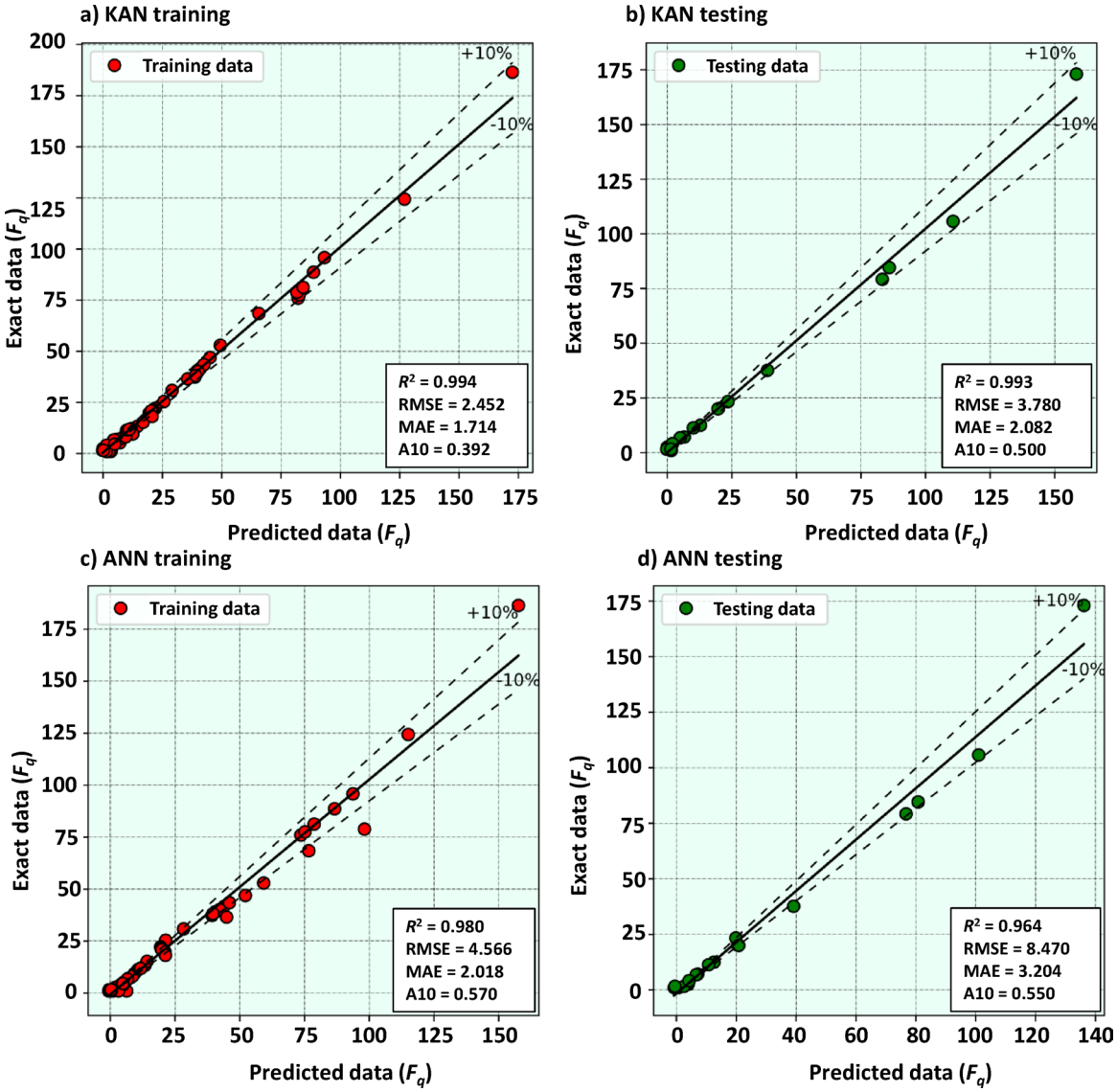

Fig. 31. Regression plots for F_q: (**a**) KAN with training data; (**b**) KAN with testing data; (**c**) ANN with training data; (**d**) ANN with testing data.

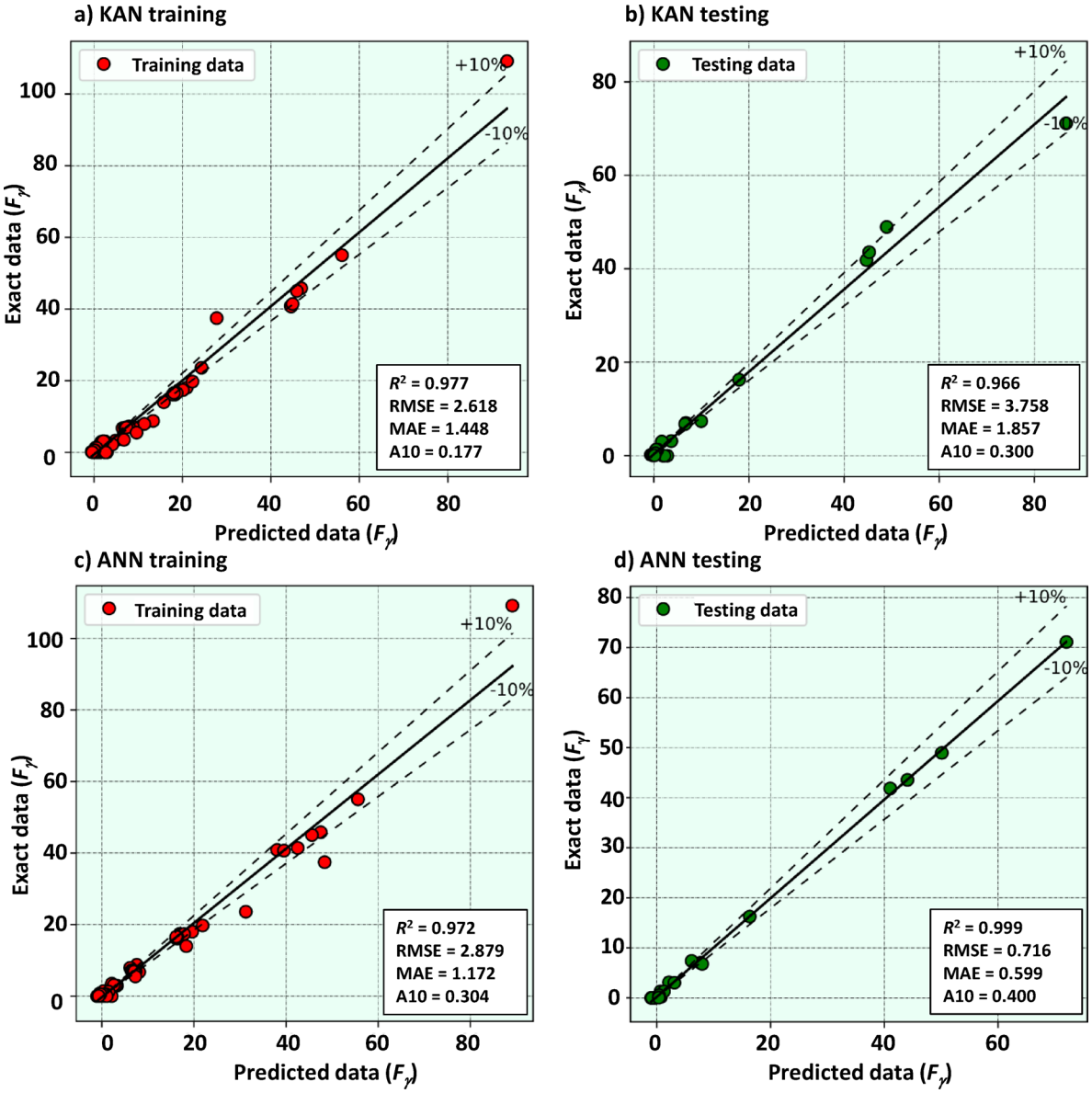

Fig. 32. Regression plots for F_γ: (**a**) KAN with training data; (**b**) KAN with testing data; (**c**) ANN with training data; (**d**) ANN with testing data.

KAN demonstrates superior computational efficiency, parameter compactness, and interpretability, validating its advantage as a data-driven surrogate for complex geotechnical modeling.

Sensitivity analysis

SHAP (SHapley Additive exPlanations) values are used to interpret the predictive behavior of the KAN model and quantify the relative importance of each input variable. SHAP provides a unified measure of feature contribution based on cooperative game theory, allowing transparent interpretation of how variations in the internal friction angle (ϕ) and the geometric ratio (r_1/B) influence the stability factors.

The SHAP values for r_1/B indicate its relatively minor influence on the bearing-capacity factors, as illustrated in Fig. 33. For F_c, F_q, and F_γ, the SHAP magnitudes of 2.06, 5.17, and 7.46 respectively show that the geometric ratio r_1/B plays a secondary role in model prediction. In contrast, the SHAP values for ϕ (11.14 for F_γ, 22.76 for F_q, and 26.77 for F_c) reveal its dominant contribution, confirming that the internal friction angle exerts the primary control on the stability coefficients. These findings emphasize that accurate determination of ϕ in soil testing is crucial for improving prediction reliability.

To further confirm the robustness of these findings, an additional *Spearman's rank correlation analysis* was performed between the input variables (ϕ, r_1/B) and the predicted stability factors (F_c, F_q, F_γ). This non-parametric test verifies the monotonic relationships without assuming linearity and provides a complementary statistical perspective to the SHAP analysis. The results, presented in Table 7, show strong and significant positive correlations between ϕ and all three stability factors, while r_1/B exhibits weak and statistically insignificant

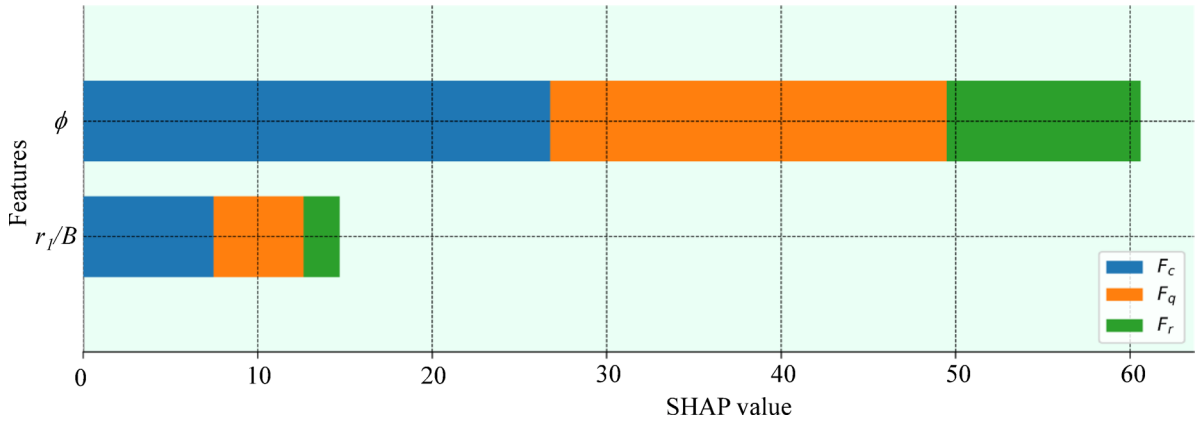

Fig. 33. SHAP values for key input variables.

Output	Variable	Spearman's ρ	*p*-value	Interpretation
(F_c)	(r_1/B)	−0.1390	0.1700	Not significant
(F_c)	(ϕ)	**0.9892**	**0.0000**	Strong positive, significant
(F_q)	(r_1/B)	−0.1061	0.2961	Not significant
(F_q)	(ϕ)	**0.9940**	**0.0000**	Strong positive, significant
(F_γ)	(r_1/B)	−0.0972	0.3387	Not significant
(F_γ)	(ϕ)	**0.9942**	**0.0000**	Strong positive, significant

Table 7. Spearman's rank correlation between input variables and predicted stability factors.

correlations. These trends are fully consistent with the SHAP results, confirming the dominant role of ϕ and the marginal influence of r_1/B.

This agreement between two independent approaches—game-theoretic (SHAP) and statistical (Spearman's ρ)—demonstrates the reliability of the model interpretation. Hence, SHAP analysis alone provides a comprehensive and physically consistent explanation of feature importance, with the correlation analysis serving as validation of interpretive robustness.

Mathematical modeling for hand calculation

In this section, we provide mathematical models for evaluating the bearing capacity factors F_c, F_q, and F_γ for ring footings on frictional-cohesive soils. These models are formulated to facilitate hand/spreadsheet calculations, making them accessible for practical engineering applications. The variables used in the models include the ratio of the internal radius to the width of the ring footing r_1/B and the internal friction angle ϕ.

Bearing capacity factor for cohesion F_c defined in Eq. (5)

$$Term1 = -0.0638\left[-0.69562(1-0.07561{}^{r_1}/_{B})^4 - 0.02152\,|(9.96608\phi + 10.0)| - 1\right]^3, \tag{3}$$

$$Term2 = -10.89874\left[-(1-0.07279{}^{r_1}/_{B})^4 + 0.04742(1-0.10667\phi)^3 + 0.28253\right]^3, \tag{4}$$

$$F_c = Term1 + Term2 + 6.95628, \tag{5}$$

Bearing capacity factor for surcharge F_q defined in Eq. (8)

$$Term1 = 11.70904\left[-0.66769(1-0.07987{}^{r_1}/_{B})^4 + 0.02743(1-0.12958\phi)^3 + 1\right]^4, \tag{6}$$

$$Term2 = 7.43219\left[-0.60353(1-0.05389{}^{r_1}/_{B})^4 - 0.06259(1-0.17666\phi)^2 - 1\right]^2, \tag{7}$$

$$F_q = Term1 + Term2 - 17.43501, \tag{8}$$

Bearing capacity factor for internal friction F_γ defined in Eq. (11)

$$Term1 = 0.86804\left[-(1-0.09719{}^{r_1}/_{B})^4 + 0.02489(1-0.13818\phi)^3 + 0.15222\right]^4, \tag{9}$$

$$Term2 = -0.19155\left[0.00109\,|(8.007200241088887{}^{r_1}/_{B} - 9.59976005554199)| - 0.01455|(9.8\phi + 10.0)|^2 + 1\right]^3, \tag{10}$$

$$F_\gamma = Term1 + Term2 + 0.16954, \tag{11}$$

These mathematical models offer an efficient and accurate approach to estimating the bearing capacity factors (F_c, F_q, and F_γ) for ring footings. The terms are carefully derived to capture the complex interactions between the ring geometry r_1/B and the internal friction angle ϕ.

For enhanced precision, the closed-form solutions derived from the optimal models provide a comprehensive representation of the underlying relationships. However, these solutions may be lengthy and less convenient for manual computations. The detailed formulations of the three models are presented below:

Bearing capacity factor for cohesion F_c.

$$Term1 = -10.13026\left[-(1-0.13508^{r_1}/_B)^4 - 0.40504(1-0.06896\phi)^2 + 0.49715\right]^4,$$
$$Term2 = 0.37083\left[-0.15285(1-0.10956^{r_1}/_B)^2 - (1-0.06513\phi)^2 + 0.40528\right]^4,$$
$$Term3 = 19.64236\left[-(1-0.07807^{r_1}/_B)^4 - 0.23876(1-0.08379\phi)^2 + 0.61851\right]^4,$$
$$Term4 = 0.31397\left[0.92223(1-0.07677^{r_1}/_B)^4 + 0.01157\left|(9.04059\phi - 2.41616)\right| - 1\right]^4,$$
$$Term5 = 10.34505\left[-0.06678(1-0.07002^{r_1}/_B)^4 - 0.97501(-0.01977\phi - 1)^2 + 1\right]^2,$$
$$Term6 = 1.93625\left[0.54467(1-0.04037^{r_1}/_B)^4 - 0.27405(1-0.07949\phi)^2 + 1\right]^2,$$
$$F_c = Term1 + Term2 + Term3 + Term4 + Term5 + Term6 + 3.61483,$$

Bearing capacity factor for surcharge F_q.

$$Term1 = -13.58928\left[-(1-0.13508^{r_1}/_B)^4 - 0.40504(1-0.06896\phi)^2 + 0.52386\right]^4,$$
$$Term2 = 0.47247\left[-0.11743(1-0.10956^{r_1}/_B)^2 - 0.76824(1-0.06513\phi)^2 - 1\right]^4,$$
$$Term3 = 26.66284\left[-(1-0.07807^{r_1}/_B)^4 - 0.23876(1-0.08379\phi)^2 + 0.65227\right]^4,$$
$$Term4 = 1.63673\left[0.64472(1-0.07677^{r_1}/_B)^4 + 0.00809abs\,(9.04059\phi - 2.41616) - 1\right]^3,$$
$$Term5 = 5.26178\left[-0.0685(1-0.07002^{r_1}/_B)^4 - (-0.01977\phi - 1)^2 + 0.70035\right]^2,$$
$$Term6 = 1.20231\left[0.45264(1-0.04037^{r_1}/_B)^4 - 0.22774(1-0.07949\phi)^2 + 1\right]^3,$$
$$F_q = Term1 + Term2 + Term3 + Term4 + Term5 + Term6 - 4.68675,$$

Bearing capacity factor for internal friction F_γ.

$$Term1 = -2.91036\left[-0.15285(1-0.10956^{r_1}/_B)^2 - (1-0.06513\phi)^2 + 0.75423\right]^3,$$
$$Term2 = 8.56791\left[-(1-0.07807^{r_1}/_B)^4 - 0.23876(1-0.08379\phi)^2 + 0.66867\right]^4,$$
$$Term3 = -0.34648\left[0.44135(1-0.07677^{r_1}/_B)^4 + 0.00554abs\,(9.04059\phi - 2.41616) - 1\right]^3,$$
$$Term4 = 14.572\left[-0.04848(1-0.07002^{r_1}/_B)^4 - 0.7078(-0.01977\phi - 1)^2 + 1\right]^2,$$
$$Term5 = 0.46172\left[0.56268(1-0.04037^{r_1}/_B)^4 - 0.28311(1-0.07949\phi)^2 + 1\right]^4,$$
$$Term6 = -0.04161\left|\left[7.36851(0.13508^{r_1}/_B - 1)^4 + 2.98455(0.06896\phi - 1)^2 + 2.95817\right]\right|,$$
$$F_\gamma = Term1 + Term2 + Term3 + Term4 + Term5 + Term6 - 1.4999,$$

These detailed equations are provided to ensure accuracy and reproducibility in advanced computational applications, while simplified versions can be used for practical engineering purposes. The derived closed-form KAN-based equations for the stability factors (F_c, F_q, and F_γ) therefore serve as a practical and efficient tool for preliminary design and hand-calculation of ring footings on frictional–cohesive soils under surcharge loading. Once the internal friction angle (ϕ) and the geometric ratio (r_1/B) are specified, these equations enable rapid estimation of ultimate bearing capacity without requiring iterative finite element limit analyses. Within the trained input domain, the predicted results agree with FELA outputs within approximately 3–5%, confirming their adequacy for conceptual and early-stage design use. Their compact analytical forms can be readily implemented in geotechnical design spreadsheets or educational exercises, facilitating quick evaluation of stability factors, sensitivity to key parameters, and comparison of design alternatives. This integration of data-driven modeling and engineering usability effectively bridges the gap between advanced computational methods and routine geotechnical practice.

Conclusions

This study rigorously revisited the bearing-capacity problem of ring footings on frictional–cohesive soils with surcharge by integrating Terzaghi's three-factor framework with modern finite-element limit analysis. The numerical results were validated against established published solutions, confirming their accuracy and reliability. The analysis also provided a detailed insight into the failure mechanisms of ring footings under varying geometric and soil conditions, contributing to a comprehensive understanding of their stability behavior.

A key innovation of this research lies in the successful development and application of Kolmogorov–Arnold Networks (KAN) for predicting the bearing-capacity factors of ring footings. Quantitatively, the KAN achieved R^2 = 0.998 (training) and 0.992 (testing) for predicting F_c, outperforming the benchmark Artificial Neural Network (ANN) (R^2 = 0.987 and 0.972, respectively). The KAN also produced lower error metrics (RMSE = 1.78, MAE = 1.199 for training) compared with the ANN (RMSE = 4.302, MAE = 1.198). Overall, KAN exhibited superior predictive accuracy and parameter efficiency for F_c and F_q, whereas the ANN showed a marginal advantage for F_γ. This nuanced outcome highlights that while KAN offers enhanced compactness and interpretability, model performance may vary depending on the stability factor considered.

The interpretability analysis based on SHAP values, supported by Spearman's rank correlation verification, identified the internal friction angle (ϕ) as the most influential parameter governing bearing-capacity factors, followed by the geometric ratio (r_1/B) with a secondary effect. These results emphasize the importance of accurate characterization of ϕ in both experimental testing and numerical modeling to ensure reliable design predictions.

In summary, this study advances the understanding of ring-footing behavior on frictional–cohesive soils through a data-driven reinterpretation of Terzaghi's stability factors. The integration of KAN with limit analysis establishes a transparent, efficient, and physically consistent predictive framework, providing both theoretical insight and practical value for geotechnical design. The demonstrated methodology offers a promising foundation for extending KAN-based modeling to other complex geotechnical systems.

Data availability

The authors confirm that the data supporting the findings of this study are available within the article [and/or] its supplementary materials.

Received: 6 January 2025; Accepted: 9 December 2025
Published online: 21 December 2025

References

1. Prasad, S. D. & Chakraborty, M. Bearing capacity of ring footing resting on two layered soil. *Comput. Geotech.* **134**, 104088. https://doi.org/10.1016/j.compgeo.2021.104088 (2021).
2. Seyedi Hosseininia, E. Bearing capacity factors of ring footings. *Iran. J. Sci. Technol. Trans. Civil Eng.* **40**, 121–132. https://doi.org/10.1007/s40996-016-0003-6 (2016).
3. Fisher, K. Zur berechnung der Setzung von fundamenten in der form einer kreisformigen ringflache. *Der Bauingenieur*. **32**, 172–174 (1957).
4. Egorov, K. in Proc. 6 th international conference of soil mechanics and foundation engineering. 41–45.
5. Egorov, K. & Nichiporovich, A. in Proceedings of the 5th international conference on soil mechanics and foundation engineering. 861–866.
6. Milovic, D. in Proc., 8th Int. Conf. on Soil Mechanics and Foundation Engineering. 167–171.
7. Al-Sanad, H. A., Ismael, N. F. & Brenner, R. P. Settlement of circular and ring plates in very dense calcareous sands. *J. Geotech. Eng.* **119**, 622–638. https://doi.org/10.1061/(asce)0733-9410 (1993). (1993)119:4(622).
8. Ismael, N. F. Loading tests on circular and ring plates in very dense cemented sands. *J. Geotech. Eng.* **122**, 281–287. https://doi.org/10.1061/(asce)0733-9410(1996)122:4(281) (1996).
9. Saha, M. Ultimate bearing capacity of ring footings on sand. M. Eng. thesis (1978).
10. Boushehrian, J. & Hataf, N. Experimental and numerical investigation of the bearing capacity of model circular and ring footings on reinforced sand. *Geotext. Geomembr.* **21**, 241–256. https://doi.org/10.1016/s0266-1144(03)00029-3 (2003).
11. Zhao, L. & Wang, J. H. Vertical bearing capacity for ring footings. *Comput. Geotech.* **35**, 292–304. https://doi.org/10.1016/j.compgeo.2007.05.005 (2008).
12. Kumar, J. & Chakraborty, M. Bearing Capacity Factors for Ring Foundations. *J. Geotech. GeoEnviron. Eng.* **141**, https://doi.org/10.1061/(asce)gt.1943-5606.0001345 (2015).
13. Keshavarz, A. & Kumar, J. Bearing capacity computation for a ring foundation using the stress characteristics method. *Comput. Geotech.* **89**, 33–42. https://doi.org/10.1016/j.compgeo.2017.04.006 (2017).
14. Tang, C. & Phoon, K. K. Prediction of bearing capacity of ring foundation on dense sand with regard to stress level effect. *Int. J. Geomech.* **18** https://doi.org/10.1061/(asce)gm.1943-5622.0001312 (2018).
15. Bui-Ngoc, T., Nguyen, T., Nguyen-Quang, M. T. & Shiau, J. Predicting load-displacement of driven PHC pipe piles using stacking ensemble with Pareto optimization. *Eng. Struct.* **316** https://doi.org/10.1016/j.engstruct.2024.118574 (2024).
16. Nguyen, T., Ly, D. K., Shiau, J. & Nguyen-Dinh, P. Optimizing load-displacement prediction for bored piles with the 3mSOS algorithm and neural networks. *Ocean Eng.* **304**, 117758. https://doi.org/10.1016/j.oceaneng.2024.117758 (2024).
17. Nguyen-Minh, T., Bui-Ngoc, T., Shiau, J., Nguyen, T. & Nguyen-Thoi, T. Undrained sinkhole stability of circular cavity: a comprehensive approach based on isogeometric analysis coupled with machine learning. *Acta Geotech.* https://doi.org/10.1007/s11440-024-02266-3 (2024).
18. Shiau, J., Nguyen, T. & Ly-Khuong, D. Unraveling seismic uplift behavior of plate anchors in frictional-cohesive soils: A comprehensive analysis through stability factors and machine learning. *Ocean Eng.* **297**, 116987. https://doi.org/10.1016/j.oceaneng.2024.116987 (2024).
19. Nguyen, D. K., Nguyen, T. P., Ngamkhanong, C., Keawsawasvong, S. & Lai, V. Q. Bearing capacity of ring footings in anisotropic clays: FELA and ANN. *Neural Comput. Appl.* **35**, 10975–10996. https://doi.org/10.1007/s00521-023-08278-6 (2023).
20. Vali, R. et al. Developing a novel big dataset and a deep neural network to predict the bearing capacity of a ring footing. Journal of Rock Mechanics and Geotechnical Engineering, (2024). https://doi.org/10.1016/j.jrmge.2024.02.016
21. Kolmogorov, A. N. *On the representation of continuous functions of several variables by superpositions of continuous functions of a smaller number of variables* (American Mathematical Society, 1961).
22. Kolmogorov, A. N. On the representation of continuous functions of many variables by superposition of continuous functions of one variable and addition. *Translations Am. Math. Soc.* **2**, 55–59 (1963).
23. Liu, Z. et al. Kan: Kolmogorov-arnold networks. arXiv preprint arXiv:2404.19756 (2024).
24. Bolton, M. D. & Lau, C. K. Vertical bearing capacity factors for circular and strip footings on Mohr–Coulomb soil. *Can. Geotech. J.* **30**, 1024–1033. https://doi.org/10.1139/t93-099 (1993).
25. Davis, E. & Booker, J. in Proc. 1st Australian-New Zealand Conf. on Geomechanics, Melbourne. 275–282.
26. Shiau, J., Keawsawasvong, S. & Yodsomjai, W. Determination of support pressure for the design of square box culverts. *Int. J. Geomech.* **23** https://doi.org/10.1061/(asce)gm.1943-5622.0002620 (2023).
27. Nguyen, T. & Shiau, J. Revisiting active and passive Earth pressure problems using three stability factors. *Comput. Geotech.* **163**, 105759. https://doi.org/10.1016/j.compgeo.2023.105759 (2023).
28. Krabbenhoft, K., Lyamin, A. & Krabbenhoft, J. Optum computational engineering (OptumG2). Computer software (2015).
29. Gholami, H. & Hosseininia, E. S. Bearing capacity factors of ring footings by using the method of characteristics. *Geotech. Geol. Eng.* **35**, 2137–2146. https://doi.org/10.1007/s10706-017-0233-9 (2017).
30. Chavda, J. T. & Dodagoudar, G. R. Finite element evaluation of vertical bearing capacity factors N'_c, N'_q, N'_γ for ring footings. *Geotech. Geol. Eng.* **37**, 741–754. https://doi.org/10.1007/s10706-018-0645-1 (2018).
31. Benmebarek, S., Remadna, M. S., Benmebarek, N. & Belounar, L. Numerical evaluation of the bearing capacity factor of ring footings. *Comput. Geotech.* **44**, 132–138. https://doi.org/10.1016/j.compgeo.2012.04.004 (2012).
32. Mangalathu, S., Hwang, S. H. & Jeon, J. S. Failure mode and effects analysis of RC members based on machine-learning-based SHapley additive explanations (SHAP) approach. *Eng. Struct.* **219**, 110927. https://doi.org/10.1016/j.engstruct.2020.110927 (2020).

Acknowledgements

AcknowledgementsThe authors also sincerely thank the anonymous reviewers for their valuable comments and suggestions, which have substantially improved the quality of this work.

Author contributions

Tran Vu-Hoang: Methodology, Investigation, Formal analysis, Data Curation, Writing - Original Draft, Writing - Review & Editing; Tan Nguyen: Conceptualization, Formal analysis, Investigation, Data Curation, Writing - Original Draft, Writing - Review & Editing, Supervision; Jim Shiau: Conceptualization, Methodology, Investigation, Writing - Review & Editing, Validation; Duy Ly-Khuong: Visualization, Formal analysis, Methodology; Hung-Thinh Pham-Tran: Formal analysis, Data curation, Visualization.

Funding

This research received no specific grant from any funding agency in the public, commercial, or not-for-profit sectors.

Declarations

Competing interests

The authors declare no competing interests.

Additional information

Supplementary Information The online version contains supplementary material available at https://doi.org/10.1038/s41598-025-32268-4.

Correspondence and requests for materials should be addressed to T.N.

Reprints and permissions information is available at www.nature.com/reprints.

Publisher's note Springer Nature remains neutral with regard to jurisdictional claims in published maps and institutional affiliations.